JTTEE5 5:401-418
©ASM International

Residual Stresses in Thermal Spray Coatings and Their Effect on Interfacial Adhesion: A Review of Recent Work

T.W. Clyne and S.C. Gill

An overview is presented of the development of residual stresses in thermal spray coatings and their effects on interfacial debonding. The main experimental techniques for measurement of residual stresses are briefly described, with particular attention given to the method of continuous curvature monitoring. Boundary conditions satisfied by all residual stress distributions are identified and expressions derived for the curvatures and stress distributions arising from a uniform misfit strain between coating and substrate. It is noted that stress distributions in thick coatings rarely correspond to the imposition of such a uniform misfit strain, so that recourse to numerical methods becomes essential for quantitative prediction of stress distributions. Relationships are presented between residual stresses and corresponding strain energy release rates during interfacial debonding. The effect on this of superimposing stresses from an externally applied load is outlined. The initiation of debonding is then considered, covering edge effects and other geometrical considerations. Finally, some specific case histories are briefly outlined to illustrate how the various theoretical concepts involved relate to industrial practice.

Keywords adhesion, debonding, interfacial toughness, residual stresses, strain energy release rate

1. Introduction

IT IS WIDELY recognized that residual stresses in thermally sprayed coatings are highly significant in practical terms. However, although recently there have been important advances in understanding how these stresses arise and how they can influence the performance of a coating, industrial development and optimization of spraying procedures is still largely carried out with, at best, only qualitative account taken of their nature and role. In many cases, such development remains entirely empirical, with regard to control over residual stresses, and thus inefficient.

Considerable efforts have been made in recent years to understand and predict the residual stresses that develop during the production of thermally sprayed coatings. In most cases, it can be assumed that stresses in the through-thickness direction are negligible and that the stresses are the same in all directions within the plane of the coating. A single stress value thus characterizes the stress state at any given depth below the free surface. However, establishing the stress state is generally more complex for a sprayed coating than for (thin) films deposited by atomistic processes, since sprayed coatings are considerably thicker and variations in stress level with depth are often significant.

Many recent studies have focused on measurement (Ref 1-7) of residual stresses and modeling (Ref 8-13) of their development during spraying. However, in very few studies have reliable correlations been established among process conditions, measured stress levels, and indicators of coating performance. In addition, agreement between measurements made on nominally similar coatings using different methods, or indeed by different workers using the same methods, has often been poor. This has been partly a consequence of uncertainties about the depth at which the stress is being measured and the likelihood of significant variations in stress level with depth. Confusion can also be caused by use of inappropriate thermophysical property data, notably the coating stiffness, which often differs substantially from handbook values and should be measured directly (Ref 14, 15).

This paper presents an overview of residual stresses associated with thermally sprayed coatings. Since inconsistencies often arise between quoted experimental values, consideration is first given to the techniques most commonly used to measure residual stresses. This is followed by an outline of the origin of residual stresses. Attention is then concentrated on the relationship between residual stresses and the interfacial adhesion between coating and substrate. Finally, the industrial significance of these concepts is highlighted by describing and interpreting several illustrative case histories.

2. Measurement of Residual Stresses

Three main types of method are commonly used to investigate residual stresses in sprayed coatings. The most direct of these involves measurement of the spacing of selected lattice planes in a crystalline structure using an x-ray beam. Although this could in principle be carried out while a coating was being deposited, in practice the experimental requirements of the method are such that it is virtually impossible during thermal spraying. This also tends to be the case for beam analysis techniques in which the nature of the reflected beam, rather than its direction, is used to deduce the stress level. Such methods include Raman spectroscopy, which has been used (Ref 16) to measure stresses in chemical vapor deposition films, but has not yet been widely applied to sprayed coatings.

T.W. Clyne, Department of Materials Science and Metallurgy, University of Cambridge, Pembroke Street, Cambridge CB2 3QZ, U.K.; and **S.C. Gill,** Sulzer Innotec AG, Postfach CH84-01 Winterthur, Switzerland.

Symbols

a (m)	half-crack length
b (m)	width of specimen
B	dimensionless constant (Eq 23)
C (m/N)	specimen compliance
E (Pa)	Young's modulus
E' (Pa)	effective Young's modulus
G (J/m^2)	strain energy release rate
h (m)	deposit thickness
H (m)	substrate thickness
K (Pa$\sqrt{\text{m}}$)	stress-intensity factor
K (W/m · K)	thermal conductivity
L (m)	length of substrate or span between inner loading points (Fig. 12)
M (N · m)	bending moment
P (N)	force
Q (W/m^2)	incident heat flux
s (m)	moment span (Fig. 12)
u (m)	displacement
x (m)	distance along the length of the beam
y (m)	distance, relative to the neutral axis, through the thickness of the beam
z (m)	distance through the width of the beam

Greek symbols

α (K^{-1})	thermal expansivity
α	Dundurs parameter (Eq 24)
δ (m)	displacement of neutral axis from interface
γ	dimensionless constant (Eq 10)
Γ	ratio of shear moduli (Eq 10)
ε	strain
$\Delta\varepsilon$	misfit strain (between stress-free dimensions of substrate and deposit)
κ (m^{-1})	curvature in x-y plane
$\Delta\kappa$ (m^{-1})	change in curvature on debonding
ν	Poisson ratio
ψ	dimensionless constant (Eq 10)
ψ	phase angle of complex stress-intensity factor
σ (Pa)	stress
Σ (Pa · m^4)	flexural stiffness (of a beam)

Subscripts

B	bifurcation
c	critical value
d, s, c	deposit, substrate, and composite parts of the specimen, respectively
i	interfacial
p, r, pr	type of strain energy release rate; p is due to the applied load only, r is due to the residual stress only, and pr is due to both.
x, y, z	orthogonal directions: x is parallel to the direction of crack propagation, y is normal to the plane of the crack, and z is parallel to the crack front.

The remaining methods do not depend on direct sensing of the strain between lattice planes or individual atoms, but rather involve detecting macroscopic shape changes that arise as a consequence of the stresses. These can be divided into material removal methods, in which changes in in-plane strain are measured (usually via strain gages) while nearby parts of the specimen are physically removed, and curvature methods, in which surface curvatures are monitored. In both cases, measurement is straightforward, but interpretation of the data to obtain stress distributions may be more complex. Curvature monitoring has the important advantage of being nondestructive and applicable while deposition is taking place.

2.1 *Diffraction Methods*

The most popular method for direct measurement of residual stresses is monitoring of the shift of selected x-ray diffraction (XRD) peaks (Ref 1, 3-5, 9, 12, 17). The principle is depicted schematically in Fig. 1. The method is applicable only to materials with well-defined crystal structures and becomes difficult (as a result of peak broadening) when the grain size is very fine or if unpredictable variations in composition are likely to occur. The lattice strain is obtained from the shift of an *hkl* peak, when compared with that for a corresponding unstrained specimen. Although the lattice strain, and hence stress, in a selected in-plane (x) direction can in principle be estimated via the Bragg equation from a single measurement, it is more accurate to examine the variation in peak shift as a function of φ, the angle between the normal to the coating surface (y-direction) and the normal to the diffracting planes (which lies in the x-y plane). The stress can then be obtained from

$$\sigma_x = \left(\frac{E}{1+\nu}\right)_{hkl} \frac{1}{d_0}\left(\frac{\partial d}{\partial \sin^2 \varphi}\right) \qquad \text{(Eq 1)}$$

where d is the measured interplanar spacing and d_0 is the value for an unstrained sample. The Young's modulus, E, and Poisson's ratio, ν, for the *hkl* planes must be accurately known. In general, these are best obtained by experimental measurement, using a sample with a known stress state.

A number of difficulties arises from the limited penetration depth of x-rays through most coating materials of interest; typically, this is approximately 10 to 50 μm, depending on the source wavelength and coating material. First, this places a limitation on the range of φ, since large values would require the incident x-ray beam to penetrate through appreciable thicknesses of coating and/or substrate. Second, the penetration depth is usually no greater than the surface roughness of as-sprayed coatings. Thus, strains are being measured within a region that is subject to substantial stress relaxation, associated with the free surfaces inclined to the coating plane. Further errors arise from variations in the stress level with depth. Attempts to explore this by successive layer-removal techniques (Ref 5) present problems, since such removal itself changes the stress distribution, even if it can be effected without inducing any deformation or damage in the underlying material (see section 2.2).

An alternative to XRD is the use of neutrons (Ref 18). Since neutrons can penetrate large distances through most materials, and collimation techniques can allow depth profiling, most of the drawbacks to the use of x-rays can be overcome. Unfortunately, scattering intensities tend to be relatively low, so that it is very difficult to obtain sufficient data in a reasonable time from small volumes, such as those of interest in coatings. Also, the availability of neutron sources is limited. Consequently, the method has not yet been extensively applied to coatings, although work in this area is now under way (Ref 19).

2.2 *Material Removal Methods*

There are two basic methods involving material removal: Either a hole can be drilled in the specimen (Ref 20, 21) or layers can be removed by polishing (Ref 13). The latter technique is illustrated in Fig. 2, which shows schematically how the new stress state in the remaining part of the specimen, and hence the strain gage reading, are related to the change in axial force and bending moment induced by the removal. For both methods, measurements are made via strain gages, which are usually attached to the uncoated side of the substrate. Whichever method is employed, there are basically two sets of problems. First, there are the physical problems of removing material in a controlled manner. If the removal induces plastic deformation or damage, then the assumption of a linear elastic change in stress state becomes invalid. Removal without damage is particularly difficult for ceramic coatings. Furthermore, as removal is effected, and indeed in many cases before any removal has occurred, the specimen is likely to adopt significant curvature. This makes the removal of a layer of uniform thickness physically very difficult. Second, it is not a simple matter to analyze the strain gage data so as to obtain the initial stress distribution. Numerical methods generally are necessary. Nevertheless, the method can apparently produce convincing results in some cases (Ref 13).

2.3 *Curvature Methods*

Probably the most informative method of residual stress evaluation, at least for thermally sprayed coatings, involves measuring the curvature of the substrate/deposit couple. Curvature can be measured by a variety of contacting and noncontacting techniques. In general, curvatures down to about 0.1 m^{-1} (10 m radius) are easy to measure, whereas much lower values require care and specialized equipment. However, while curvatures are often readily measured, it is a more complex task to interpret such data in terms of stress state. This is partly because, while the curvature adopted by a system with a given stress state is unique and predictable, a given curvature does not correspond to a unique stress state. However, it is possible to infer a stress distribution from a curvature, provided certain boundary conditions are assumed.

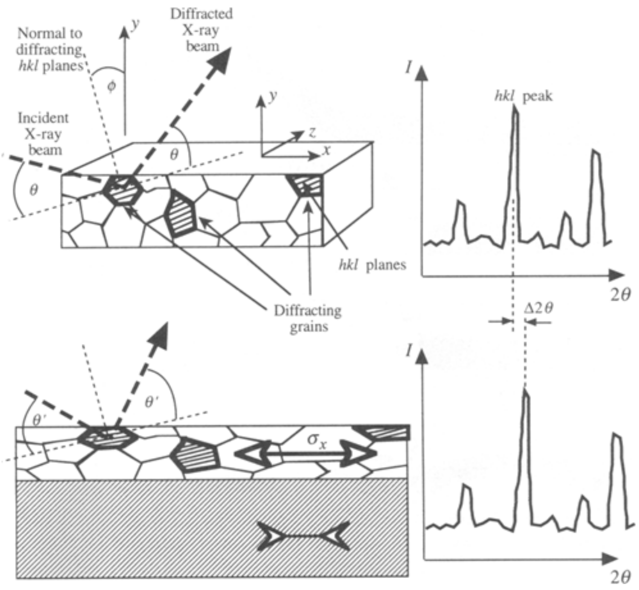

Fig. 1 Schematic of the XRD technique for measurement of residual stresses

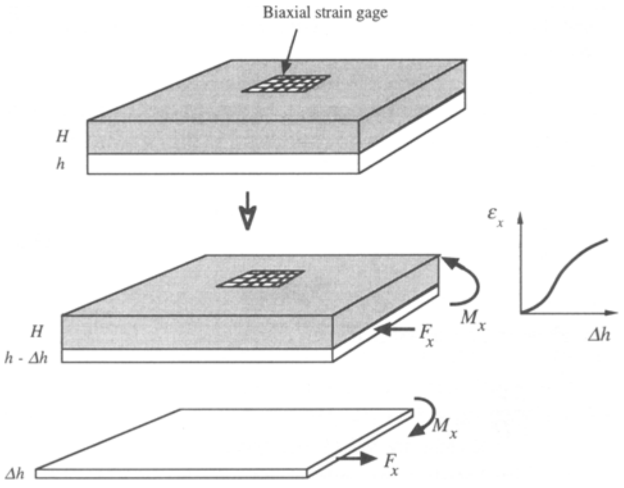

Fig. 2 Schematic of the strain gage technique for investigation of residual stress, based on layer removal

2.3.1 Force and Moment Balances

Consider a pair of plates bonded together with a misfit strain $\Delta\varepsilon$ in the x-direction (Fig. 3) (Ref 22). The resultant stress distribution, $\sigma_x(y)$, and curvature, κ, can be obtained from simple beam bending theory. First, the misfit strain is removed by the application of two equal and opposite forces ($-P$ and P). When the two plates are joined, this results in an unbalanced moment, M. Balancing this moment generates curvature of the composite plate. The moment is given by:

$$M = P\left(\frac{h+H}{2}\right) \qquad \text{(Eq 2)}$$

where h and H are the thicknesses of the deposit and substrate, respectively.

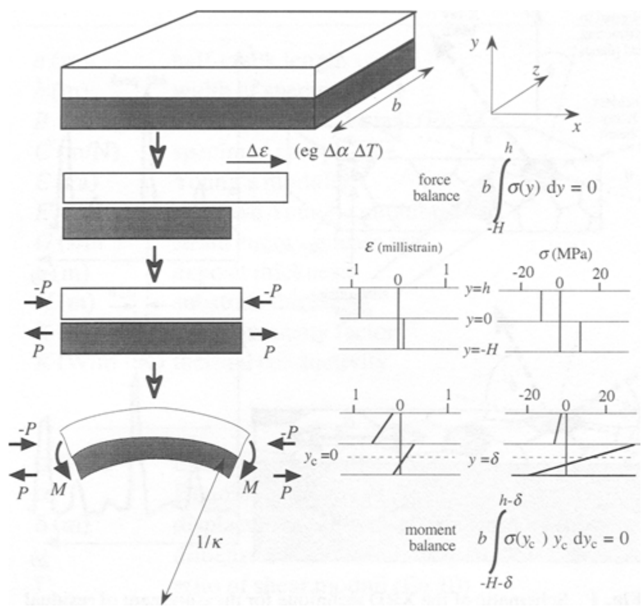

Fig. 3 Schematic of the generation of curvature in a flat bimaterial plate as a result of the imposition of a uniform, linear misfit strain, $\Delta\varepsilon$. The distributions of stress and strain shown were calculated, using Eq 12 and 13, for $H = h$, $E_S = 100$ GPa, $E_d/E_S = 0.1$, and $\Delta\varepsilon = 10^{-3}$. Source: Ref 22

Now, the curvature of a beam, κ (equal to the through-thickness gradient of strain), can be expressed as the bending moment divided by the beam stiffness, Σ:

$$\kappa = \frac{M}{\Sigma} \qquad \text{(Eq 3)}$$

so that P can be expressed as:

$$P = \frac{2\,\Sigma\,\kappa}{h + H} \qquad \text{(Eq 4)}$$

The beam stiffness of a prismatic composite beam is given by:

$$\Sigma = b\int_{-H-\delta}^{h-\delta} E(y_c)\,y_c^2\,dy_c = b\,E_d\,h\left(\frac{h^2}{3} - h\,\delta + \delta^2\right) + b\,E_s\,H\left(\frac{H^2}{3} + H\,\delta + \delta^2\right) \qquad \text{(Eq 5)}$$

where b is the specimen width, E is the Young's modulus, and δ is the distance from the neutral axis ($y_c = 0$) to the interface ($y = 0$). The value of δ is given by:

$$\delta = \frac{h^2\,E_d - H^2\,E_s}{2(h\,E_d + H\,E_s)} \qquad \text{(Eq 6)}$$

The magnitude of P is readily found from a strain compatibility condition. The misfit strain can be expressed as the sum of the strains resulting from application of the P forces:

$$\Delta\varepsilon = \varepsilon_s - \varepsilon_d = \frac{P}{H\,b\,E_s} + \frac{P}{h\,b\,E_d} \therefore \frac{P}{b} = \Delta\varepsilon\left(\frac{h\,E_d\,H\,E_s}{h\,E_d + H\,E_s}\right) \qquad \text{(Eq 7)}$$

Combination of this with Eq 4 to 6 leads to a general expression for the curvature arising from the imposition of a uniform misfit strain, $\Delta\varepsilon$, such as would arise during a change in temperature ($\Delta\varepsilon = \Delta\alpha\Delta T$):

$$\kappa = \frac{6\,E_d\,E_s\,(h + H)\,h\,H\,\Delta\varepsilon}{E_d^2\,h^4 + 4\,E_d\,E_s\,h^3\,H + 6\,E_d\,E_s\,h^2\,H^2 + 4\,E_d\,E_s\,h\,H^3 + E_s^2\,H^4} \qquad \text{(Eq 8)}$$

It may be noted that, for a given deposit/substrate thickness ratio, h/H, the curvature is inversely proportional to the substrate thickness, H. This scale effect is very important in practical terms, since relatively thin substrates are essential if curvatures sufficiently large for accurate measurement are to be generated.

2.3.2 Biaxial Stresses and Bifurcation

Equation 8 should be valid provided the original imposed misfit strain is uniform (no through-thickness gradient) and the system remains elastic while the curvature is adopted. A modification arises, however, on consideration of in-plane stresses other than those in the x-direction. For an isotropic in-plane stress state, there is effectively another stress equal to σ_x in a direction at right angles to it (z-direction); this induces a Poisson strain in the x-direction. Assuming isotropic stiffness and negligible through-thickness stress ($\sigma_y = 0$), the net strain in the x-direction can be written:

$$\varepsilon_x\,E = \sigma_x - \nu(\sigma_y + \sigma_z) = \sigma_x(1 - \nu)$$

so that the relation between stress and strain in the x-direction can be expressed as:

$$\frac{\sigma_x}{\varepsilon_x} = \frac{E}{(1 - \nu)} = E' \qquad \text{(Eq 9)}$$

This modified form of the Young's modulus, E', is usually applicable in expressions referring to substrate/coating systems having an equal biaxial stress state.

A further point related to biaxial stresses concerns the possibility of the multidirectional curvatures leading to mechanical instability. Under an equal biaxial stress state, an initially plane surface will tend to become convex or concave, with a curvature that should be equal in all directions (i.e., a spherical surface). However, high curvatures cannot be simultaneously accommodated in all in-plane directions. On increasing the curvature sufficiently, a bifurcation point will be reached, at which the curvature increases sharply in one plane and decreases sharply in the plane normal to this (i.e., the shape becomes ellipsoidal and approaches that of a cylinder). Once a specimen has bifurcated, it is difficult to reliably relate a measured curvature to an internal stress distribution.

In general, it is a complex problem to predict the curvature at the bifurcation point for a substrate/deposit system under residual stress. However, the case of a thin film on a thick, rectangular substrate (with a uniform stress in the film) has been analyzed (Ref 23). The critical curvature depends on the elastic constants, deposit/substrate thickness ratio (*h*/*H*), substrate thickness/length ratio (*H*/*L*), substrate width/length ratio (*b*/*L*), and substrate length (*L*). The magnitude of the curvature at the bifurcation point is given by (Ref 23):

$$\kappa_B = \frac{1}{L}\left(\frac{H}{L}\right)\left\{12\,\gamma\left(\Gamma\left(\frac{h}{H}\right)^2 - 1\right)^2 + 48\,\gamma\,\Gamma\left(\frac{h}{H}\right)\left(1+\left(\frac{h}{H}\right)\right)^2\right\}^{1/2} \tag{Eq 10}$$

in which Γ is the ratio of the shear moduli (G_d/G_s) and γ is a dimensionless constant evaluated from:

$$\gamma = \frac{4\left\{\Gamma\left(\frac{h}{H}\right)\psi_d + \psi_s\right\} + 5\left\{\Gamma\left(\frac{h}{H}\right)(\psi_d + 1) + \psi_s + 1\right\}\left\{\left(\frac{L}{b}\right)^2 + \left(\frac{b}{L}\right)^2\right\}}{2\left\{\Gamma\left(\frac{h}{H}\right)\psi_d + \psi_s\right\}\left\{\Gamma\left(\frac{h}{H}\right) + 1\right\}^2\left(\frac{b}{L}\right)^2}$$

where ψ_d is $(1 + \nu_d)/(1 - \nu_d)$ and ψ_s is $(1 + \nu_s)/(1 - \nu_s)$. Behavior predicted by Eq 10 is shown in Fig. 4. The critical curvature reduces as the substrate length is increased and as the width/length ratio increases. It is relatively insensitive to the elastic properties and to the deposit/substrate thickness ratio. It can be seen from the plot that there will be little or no danger of a bifurcation instability (i.e., $\kappa_B > \sim 10\ \text{m}^{-1}$) if a long ($L \sim 100$ mm), fairly narrow ($b/L < \sim 0.2$) strip specimen is used. This is convenient, since such specimens are well suited to accurate measurement of curvature along the length of the strip.

2.3.3 Thick and Thin Coatings

A simplified form of Eq 8 results when the coating is much thinner than the substrate ($h \ll H$). Since the stress in the substrate then tends to become negligible, and that in the deposit will vary little as a result of curvature adoption, the misfit strain can be converted to a deposit stress, σ_d ($=E_d\Delta\varepsilon$), so that the equation reduces to the form:

$$\kappa = \frac{6\,\sigma_d\,(1 - \nu_s)h}{E_s H^2} \tag{Eq 11}$$

which is usually known as Stoney's equation and is commonly used to relate stress to curvature for thin coatings.

When the condition $h \ll H$ does not apply, then stresses and stress gradients are often significant in both constituents. Stress distributions are readily found for the simple misfit strain case outlined previously, from the values of *P* and κ, using these expressions:

$$\sigma_d \big|_{y=h} = \frac{-P}{b\,h} + E_d\,\kappa(h - \delta) \tag{Eq 12a}$$

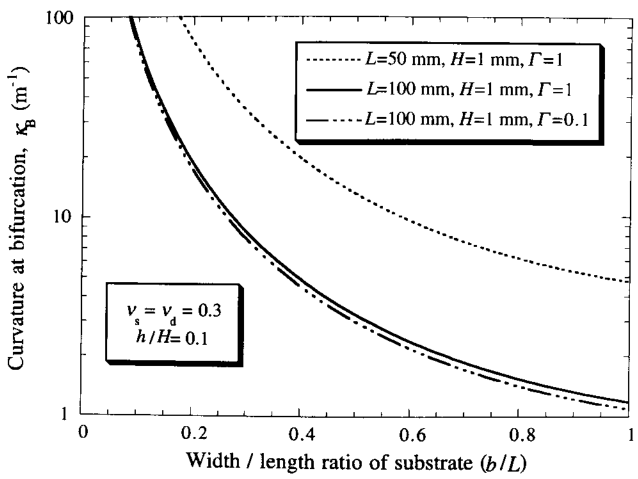

Fig. 4 Predicted dependence on width/length ratio of the critical curvature at a bifurcation instability for a residually stressed thin film on a substrate, according to Eq 10

$$\sigma_d \big|_{y=0} = \frac{-P}{b\,h} - E_d\,\kappa\delta \tag{Eq 12b}$$

$$\sigma_s \big|_{y=-H} = \frac{P}{b\,h} - E_s\,\kappa(h + \delta) \tag{Eq 13a}$$

$$\sigma_s \big|_{y=0} = \frac{-P}{b\,h} - E_s\,\kappa\delta \tag{Eq 13b}$$

The stress distributions shown in Fig. 3 were obtained using these equations. It can be seen that the adoption of curvature can effect substantial changes in stress levels and that high through-thickness gradients can result. It may be noted from Eq 12 and 13 that (for a given value of *h*/*H*), since *P* is proportional to *H* and κ is inversely proportional to *H*, the stresses at $y = -H$, 0, and *h* do not depend on *H*; that is, the stress distribution is independent of scale.

Curvature values before (κ_c) and after (κ_d and κ_s) debonding are related to the distributions of residual stress relaxed on debonding by (Ref 24):

$$\sigma_d = \frac{2\,\Sigma_d\,(\kappa_d - \kappa_c) + 2\,\Sigma_s\,(\kappa_s - \kappa_c)}{b\,h\,(h + H)} + E_d(\kappa_d - \kappa_c)y_d \tag{Eq 14}$$

$$\sigma_s = \frac{2\,\Sigma_d\,(\kappa_d - \kappa_c) + 2\,\Sigma_s\,(\kappa_s - \kappa_c)}{b\,h\,(h + H)} + E_s(\kappa_s - \kappa_c)y_s \tag{Eq 15}$$

where Σ_d and Σ_s are beam stiffnesses and y_d and y_s are distances from the respective neutral axes for deposit and substrate, respectively. These distributions are always linear in each constituent. The equations are of general validity and the approach represents a potentially powerful method for experimental investigation of residual stresses. However, its accuracy tends to be poor for thin coatings on thick substrates ($h/H \ll 1$), since when $\Sigma_s \gg \Sigma_d$ the predicted stress distribution is sensitive to observed values of ($\kappa_s - \kappa_c$), which will be small and hence difficult to measure accurately.

2.3.4 Monitoring of Curvature History

The method becomes a much more powerful one when curvatures are measured continuously during deposition. There is then scope for monitoring (and modeling) both changes in through-thickness stress gradients and the progression of inelastic processes (stress relaxation). The first description of such a continuous measurement procedure during thermal spraying was given by Kuroda et al. (Ref 25, 26). Using lightly contacting knife edges, they were able to record the changing curvature, κ, during air plasma spraying. Stoney's equation (Eq 11) was used to measure the quenching stress (see section 3.1) for several systems.

The curvature monitoring technique was then further developed by Gill and Clyne (Ref 7, 27-29), who made two advances. First, a noncontacting method of curvature measurement was employed, involving simple video recording, eliminating concern about interference with free bending of the specimen and allowing study of a wide range of substrate temperatures. Second, a numerical process model was developed (Ref 15, 27, 29-31) that allowed the curvature history to be predicted from thermomechanical boundary conditions and material property data (including the quenching stress; see section 3.1). Comparison between measured and modeled curvature (and temperature) histories provides a comprehensive method of model validation and investigation of stress generation mechanisms. Various second-order effects, such as creep of titanium substrates during deposition (Ref 32), have been successfully incorporated into the model. (An obvious point to note is that, while validation is best carried out with a thin substrate so that curvature changes during the process are relatively large, the model will then be applicable to thick substrate cases in which changes of curvature may be negligible.)

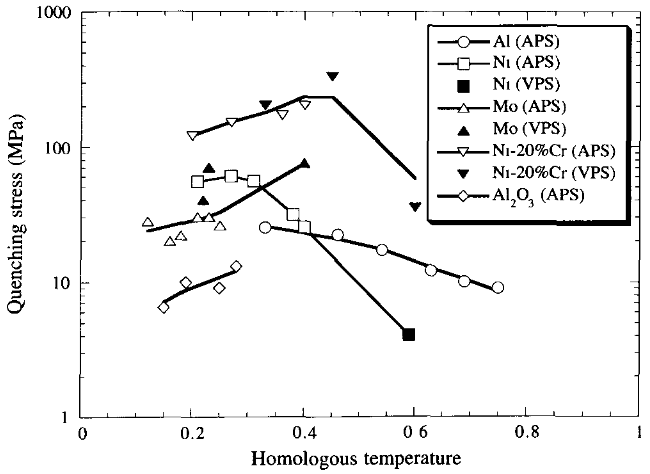

Fig. 5 Experimental quenching stresses for plasma spraying in air (APS) or in vacuum (VPS). The values are plotted against the ratio of the specimen temperature to the melting temperature of the deposit. The data were obtained from specimen curvature measurements during spraying. Source: Ref 37

3. Origin of Residual Stresses

Residual stresses in sprayed coatings arise from two main sources. First, there are the "intrinsic," "deposition," or "quenching" stresses, which are generated as the incoming splats form and cool to the current specimen temperature; second, differential thermal contraction stresses can arise as the substrate and coating subsequently change temperature together. Misfit strains rather similar to those from differential thermal contraction can arise after deposition as a result of phase changes, structural relaxation, or plastic flow—which can occur in the substrate and/or deposit. Finally, the effects of through-thickness thermal gradients are worth noting. Although a linear thermal gradient in a monolithic specimen generates curvature but no stresses, stresses will arise if the gradient is nonlinear or if there are through-thickness variations in thermal expansivity. In the latter case, residual stresses may result if these transient stresses generate inelastic effects such as plastic flow.

3.1 *Quenching Stress*

The intrinsic stress, often termed the quenching stress (Ref 33-36) for thermal spray processing, arises from the hindered contraction of the individual splats as they cool from the melting temperature to the temperature of the underlying material. Although the associated misfit strains are often large (since specimen temperatures during spraying are usually much lower than the melting temperature of the coating), quenching stress values are in many cases relatively low (<100 MPa). Experimental data are shown in Fig. 5. It can be seen that there are no significant differences between the data for plasma spraying in air or in vacuum. For other thermal spray processes, such as the high-velocity oxyfuel process, values may be slightly different as a result of different impact conditions, intersplat bond strength, and so on.

Typical maximum theoretical values for the quenching stress [$\sim E_d \alpha_d (T_{md} - T_s)$] are on the order of 1 GPa. The reason for most experimental values being low relative to this is that various stress-relaxation mechanisms can operate while the quenching process is taking place. For example, interfacial sliding can occur, while many ceramic materials undergo extensive microcracking and metallic deposits are prone to plastic yielding or creep. This explains why, depending on the strength of the metal, reductions in quenching stress occur on moving to relatively high temperatures. (Also, of course, the misfit strain tends to zero as the homologous temperature tends to unity.) At lower temperatures, all materials tend to show gradual increases with temperature, which is attributed to improvements in intersplat bonding. Microcracking is common with many ceramics, leading to very low quenching stress values. It has been confirmed experimentally (Ref 36) that the substrate material has little or no effect on quenching stress values.

3.2 *Differential Thermal Contraction*

Stresses arising from differential thermal contraction should be readily obtainable from the thermal expansivities of deposit and substrate, provided the system remains elastic. Some example predictions are presented in Fig. 6. This shows peak stress levels in the deposit as a function of the misfit strain; this is given by the product of the expansivity mismatch ($=10^{-5}$ K^{-1} in this case, which is a value typical of many systems) and the temperature drop. These data were obtained from Eq 6 to 8 and 12. Several features are apparent. First, stress levels can be high (~100 MPa) even for moderate temperature changes (~100 K). (In practice, large stresses may stimulate inelastic stress-relaxation processes; see section 3.3.) Coating stresses will tend to be higher when it is thin ($h/H = 0.1$), but it can be seen that the peak stress is not much lower for the equal thickness case (although the average stress level may well be considerably less). As expected, coating stresses are reduced when it is less stiff ($E_d/E_s = 0.1$). It can be seen in Fig. 6, however, that this reduction is not in proportion to the drop in stiffness. This is clear on examining the $E_s = 10$ GPa case, in which all stresses scale with the reduction, since the drop in stiffness applies to both constituents.

It is of interest to note the curvature changes generated by differential thermal contraction. Some predictions are shown in Fig. 7 for various material combinations and dimensions. These plots were obtained from Eq 8 using the property data in Table 1. For the reference case (1 mm of alumina on a 1 mm steel substrate), even moderate temperature changes (~100 K) lead to quite substantial curvatures (>0.1 m^{-1}), but it can be seen that the curvatures would be much lower for a thicker (10 mm) substrate. Use of a titanium substrate (lower α mismatch) or a ZrO_2 deposit (lower stiffness) would also give reduced curvatures, as would a reduced coating thickness.

A further practical point is that account should be taken of the variations in thermal expansivities with temperature when making these calculations. The misfit strain on cooling from T_1 to T_2 is given by:

$$\Delta\varepsilon = \int_{T_2}^{T_1} (\alpha_s(T) - \alpha_d(T))\mathrm{d}T \qquad \text{(Eq 16)}$$

Since many expansivities change (usually increase) significantly as the temperature is raised, large errors in the misfit strain can arise if the values are taken as constant.

3.3 *Inelastic Processes*

In some cases, stress development in the substrate and the deposit takes place elastically and can be treated according to the principles outlined in sections 2.3, 3.1, and 3.2. On this basis, the

Table 1 Thermophysical properties

	Properties				
Material	**Density (ρ), Mg/m^3**	**Young's modulus (E), GPa(a)**	**Poisson ratio (ν)**	**Thermal expansivity (α), $\mu\varepsilon$ K^{-1}**	**Thermal conductivity (K), W/m·K(a)**
Substrates					
Titanium	4.5	110	0.36	9	10
Mild steel	7.9	200	0.33	12	60
Aluminum	2.7	70	0.33	24	200
Tungsten	19.1	400	0.3	4	170
Nickel	8.9	210	0.3	13	90
Deposits					
Alumina	3.8	50	0.23	8	25
Zirconia	5.6	10	0.2	8	1.5

(a) Young's modulus and thermal conductivity values for sprayed coatings are sensitive to microstructure and hence to the spraying conditions; the values shown are typical experimental data.

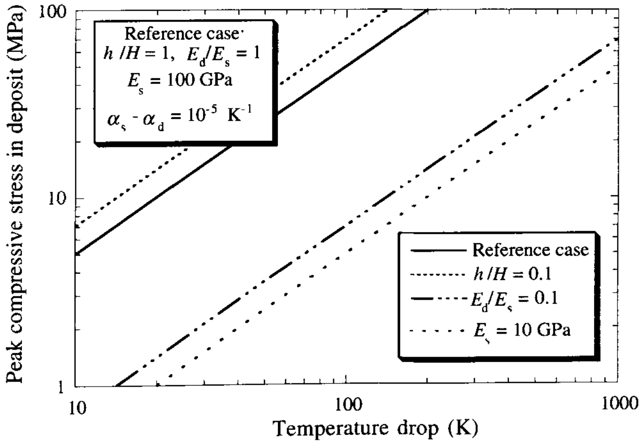

Fig. 6 Predicted peak values of the (compressive) stress in the deposit, arising from differential thermal contraction, as a function of the fall in temperature for several different cases

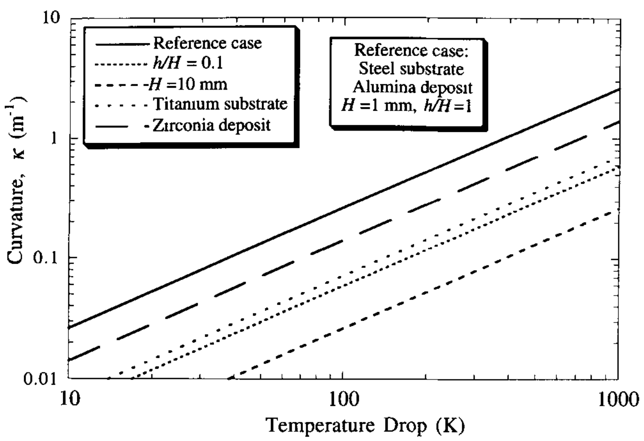

Fig. 7 Predicted curvature (with the free surface of the substrate concave) as a function of the fall in temperature for five different substrate/deposit combinations

final stress distribution (and specimen curvature) can be predicted from the (experimentally determined) value of the quenching stress and the temperature change on cooling using Eq 6 to 8, 11, 12, and 16, preferably employing a measured deposit stiffness. This calculation should be fairly reliable, provided that there is a single uniform misfit strain, $\Delta\varepsilon$, between the relaxed (stress-free) in-plane dimensions of substrate and deposit. This in turn requires that (1) the temperature and curvature of the specimen do not change appreciably during deposition (the latter requiring a thick substrate and/or a small quenching stress) and (2) no inelastic processes, such as plastic flow, creep, or microcracking, occur during deposition or subsequent cooling.

In practice, such inelastic processes are by no means uncommon. Furthermore, they often occur to varying degrees at different depths, as a result of variations in stress level and temperature. This complication, together with the fact that temperature and curvature often do change significantly during deposition, indicates that accurate modeling of stress development usually requires numerical treatment, with the stress and temperature being monitored at a series of discrete depths and times. The misfit strain, $\Delta\varepsilon$, thus becomes a time-dependent function of depth. Provided that the inelastic response characteristics (e.g., creep rate parameters) of substrate and deposit are known, then the effect of local inelastic processes can readily be incorporated into such a model, since they induce changes in the local value of $\Delta\varepsilon$ which can be calculated. Furthermore, complications such as local property changes accompanying inelastic events—for example, a reduction in stiffness associated with microcracking—can also be taken into account. It has been shown (Ref 7, 29, 30, 38) that reliable predictions can be obtained without incorporating either lateral heat flow or through-thickness stresses, so that a simple one-dimensional finite-difference or finite-element approach is satisfactory. This allows rapid recalculation of stress and temperature distributions and associated parameters such as curvature and strain energy release rates (see section 4.1), which greatly facilitates procedures such as curvature history comparisons.

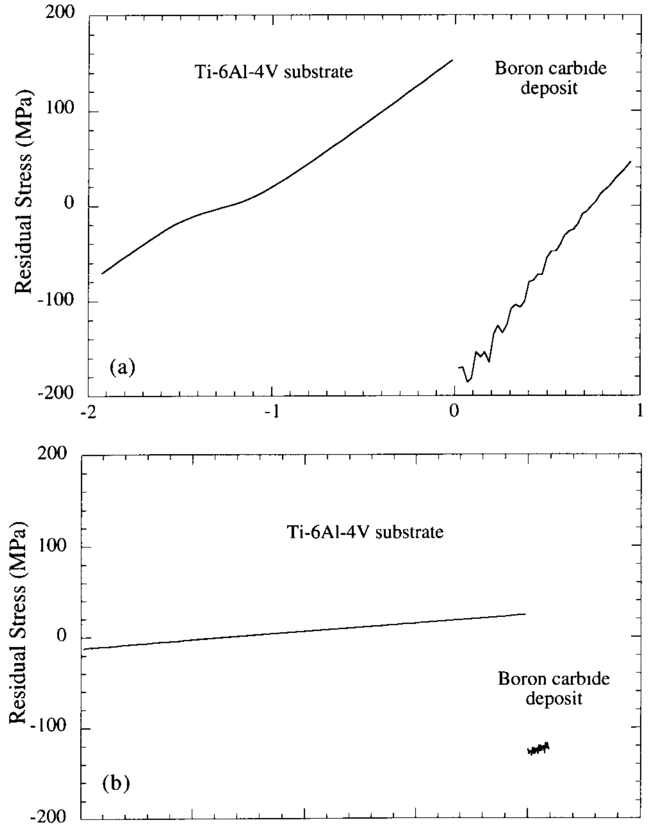

Fig. 8 Predicted residual stress distributions at room temperature after spraying of a 1 mm thick coating of B_4C onto titanium alloy substrates of thickness 2 mm (a) and 20 mm (b). A significant degree of creep has occurred in the substrate (leading to a nonlinear stress distribution) during spraying for the thin substrate, but not for the thick one. Source: Ref 32

An example of the result of such a computation is presented in Fig. 8, which shows final residual stress distributions for deposition of boron carbide onto thin or thick titanium alloy substrates (Ref 32). In this system, the most likely form of inelastic behavior is creep in the substrate. Stress levels within the thin substrate became high enough during spraying for significant creep to occur, whereas in the thick substrate they did not. This is apparent from the nonlinear substrate stress distribution in Fig. 8(a). (It may be noted that nonlinear stress profiles in the substrate arise only from inelastic processes, whereas in the deposit they can also be caused by variations in temperature or curvature during deposition.) Experimental validation of the occurrence of substrate creep for the thin substrate was provided by the improved agreement observed (Ref 32) between experimental and predicted curvature histories when creep was incorporated into the model.

3.4 *Through-Thickness Thermal Gradients*

An important feature of most thermal spraying processes is the transient injection of relatively high heat fluxes into the substrate. These cause high thermal gradients, which in turn generate differential thermal expansion at different depths and changes to the local misfit strains. Stresses and bending moments will therefore arise when the specimen is exposed to a high heat flux, although these are expected to disappear when

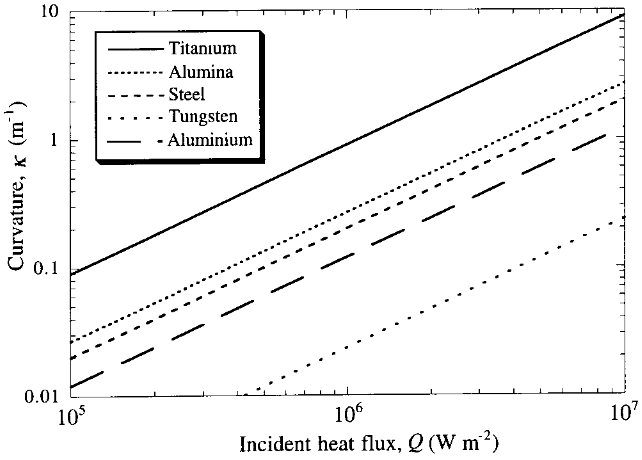

Fig. 9 Predicted curvature (with the heated surface convex) as a function of the incident heat flux for five different substrates

the thermal gradients decay, unless the stresses have in the meantime stimulated inelastic effects.

The simplest case to treat is a steady-state heat flow through a monolithic material (the substrate), giving rise to a uniform thermal gradient. This situation actually generates no stresses, since the resulting linear strain gradient will be entirely relaxed by the adoption of a corresponding curvature (assuming the specimen to be unconstrained). It is, however, useful to calculate these curvatures, since they indicate what stresses would be set up if the substrate were constrained to remain flat and also show whether curvature arising from transient heat-flow effects are likely to be significant compared with those from other sources. In this case, the curvature is given by:

$$\kappa = \frac{\alpha Q}{K} \qquad \text{(Eq 17)}$$

where Q is the incident heat flux (W/m^2) and K is the thermal conductivity (W/m · K). Predicted curvatures obtained from this equation, using property data in Table 1, are shown in Fig. 9 as a function of incident heat flux for five different substrates (with no coatings). (Values of Q range up to 10^7 W/m^2, which could be taken as a practical upper limit for normal operation; this is based on the maximum thermal power reaching a substrate being about 10 kW and the minimum substrate surface area of heat dissipation being about 1000 mm^2). It can be seen from Fig. 9 that quite large curvatures (~1 m^{-1}) might arise when the heat flux is high, although there is a strong sensitivity to the substrate material. Curvatures are high for titanium, which has a combination of low conductivity and relatively high expansivity, whereas for tungsten the reverse is the case and curvatures are always low.

4. Effect of Residual Stresses on Adhesion

In order to approach this topic systematically, it is essential to use a meaningful measure of the coating adhesion. Although a number of empirical tests have evolved to characterize spallation resistance (Ref 39), most of these do not measure a well-defined parameter of fundamental significance. The aim should be to evaluate the critical strain energy release rate for the interface, G_{ic}, or the closely related critical interfacial stress-intensity factor, K_{ic}. Recent reviews (Ref 40-46) cover factors to be considered when examining these for interfaces between dissimilar materials.

4.1 *Strain Energy Release Rates during Debonding*

Numerous studies (Ref 46-50) have focused on the relationship between residual stress distributions and corresponding strain energy release rates when the interface becomes debonded. In the simplest case of a thin coating with a uniform misfit strain, the strain energy release rate is simply the stored elastic strain energy per unit interfacial area, given by:

$$G = \frac{\sigma_d^2 h}{2E_d} + \frac{\sigma_s^2 H}{2E_s}$$

where σ_d and σ_s are the (uniform) stresses in the deposit and the substrate, respectively. Using the force balance condition relating these two stresses, this can be written as:

$$G = \frac{\sigma_d^2 h}{2E_d}\left\{1 + \left(\frac{h}{H}\right)\left(\frac{E_d}{E_s}\right)\right\} \sim \frac{\sigma_d^2 h}{2E_d} \qquad \text{(Eq 18)}$$

This can be regarded as a driving force for spontaneous debonding of the coating. It rises linearly with coating thickness. Note that the presence of other in-plane stresses has been neglected. In practice, the initial stress in the coating is often equal biaxial; in this case, both in-plane stresses will be able to relax once the film is completely debonded. However, only the stress parallel to the crack propagation direction can be relaxed as the crack tip passes the region concerned, since the other in-plane stress is still constrained. It is doubtful whether the energy released by subsequent relaxation of this stress can be efficiently fed back to the crack tip so that it can contribute to the strain energy release rate. However, it should be noted that the presence of the other in-plane stress will affect the value of G via its influence on the effective elastic modulus.

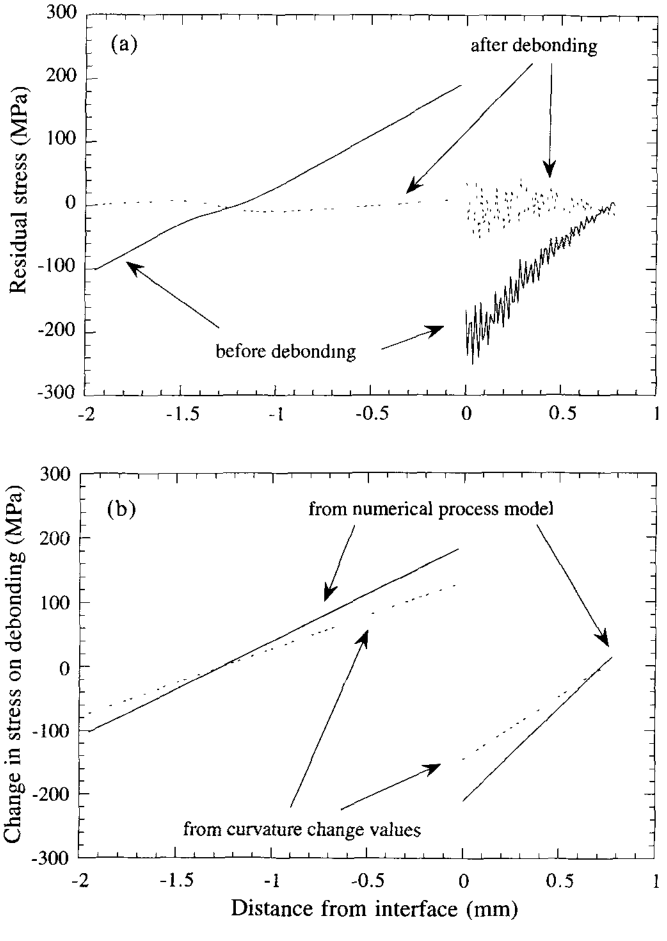

Fig. 10 (a) Predicted distribution of residual stress within a specimen composed of a thermally sprayed B_4C on a titanium alloy substrate, obtained from a numerical model of the spraying process, before and after debonding. Source: Ref 51. (b) Changes in stress on debonding, as predicted by the process model and as obtained experimentally via curvature measurements

Equation 18 can be used to estimate the critical strain energy release rate of the interface, G_{ic}, which is sometimes termed the interfacial fracture energy or the interfacial toughness. Provided that the stress in the coating is known at the point when debonding spontaneously occurs, then G_{ic} can be taken as equal to the value of G at this point. This takes no account of any barrier to the initiation of an interfacial crack and simply considers the energy balance during steady-state advance of a fully developed interfacial crack. Initiation of an interfacial crack at a specimen edge is considered in section 4.4.

For thermally sprayed coatings, a calculation based on a single deposit stress may not be acceptable for estimation of the interfacial fracture energy. Stress distributions are likely to be more complex, and it may also be inaccurate to simply calculate the total stored elastic strain energy and assume that all of this is released. In fact, only those stresses that can be relaxed by extension/contraction or bending of the coating and substrate when they are separated can contribute to G. Such stresses always form a linear profile within each constituent. To illustrate this, plots are shown in Fig. 10(a) of stress distributions in a thermally sprayed system before and after debonding of the coating. These were obtained numerically (Ref 51), using a finite-difference model of the spraying process. It can be seen that the stresses after debonding are not zero, although (as in most cases) they are fairly small.

The changes in residual stress can be converted to strain energy release rates and hence to interfacial fracture energies for cases where spontaneous debonding occurs. In Fig. 10(b), plots are shown of the changes that occurred for the example given. A comparison is shown between predictions from the numerical model and data obtained experimentally by measurement of specimen curvatures and use of Eq 14 and 15. It can be seen that there is good agreement between measured and predicted stress distributions.

The value of G can be calculated from the stress distribution at any point during spraying or subsequent cooling. Figure 11 shows variations in G for six alumina coatings on steel substrates, corresponding to different spraying temperatures and/or coating thicknesses (Ref 52). Four of these coatings debonded spontaneously before cooling to room temperature was complete, while the other two did not. It can be seen from the plot that each of the debonding events occurred when G reached the range of 400 to 500 J/m^2, while for the other two coatings this range was never attained. Since the substrate preparation procedure was the same in each case, these results are apparently consistent with the debonding event simply requiring the attainment of a critical value of G, which could be taken as G_{ic}. Although this is an attractively simple rationale, it should be noted that the picture may be complicated by variations in mode mixity (section 4.2) and by crack initiation barriers (section 4.4).

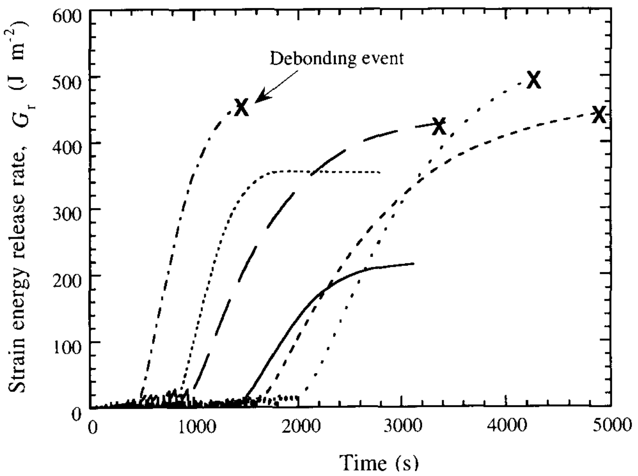

Fig. 11 Predicted variations in strain energy release rate for interfacial debonding of several alumina coatings on steel substrates during spraying and cooling. For cases when debonding took place, it occurred when G reached a critical value of approximately 400 to 500 J/m^2. Source: Ref 52

4.2 *Effect of Mode Mixity*

Analysis of interfacial debonding is complicated by the fact that the stress field at the crack tip may not represent conditions of pure crack opening (mode I). This is because, in contrast to crack propagation in a homogeneous medium, the crack is confined to a particular geometric path. Depending on the toughness of the interface and of the two media on either side, crack propagation may continue within the interface, rather than seeking a mode I path in some other direction, even though the interfacial path is heavily "mixed mode" (i.e., has a substantial shear component at the crack tip). This topic has received extensive study (Ref 24, 42-44, 53-58) in recent years. The most common method of characterizing mode mixity is to use the so-called phase angle, ψ, which is related to the crack-tip stress-intensity factors for mode I and mode II loading by:

$$\psi = \tan^{-1}\left(\frac{K_{II}}{K_I}\right) \qquad \text{(Eq 19)}$$

so that $\psi = 0°$ represents pure opening conditions and $\psi = 90°$ represents pure shear.

A major concern about mode mixity is that it could affect the fracture energy of the interface. The general expectation is that G_{ic} will rise as a shear component is introduced, since this will encourage dissipation of energy at and immediately behind the crack tip as a result of frictional rubbing between asperities. Plastic flow ahead of the crack tip may also be promoted in metallic systems. Furthermore, it is expected that roughening of the substrate surface will give rise to a more substantial increase in interfacial toughness if there is a large shear component to the crack-tip driving force.

If the dependence of G_{ic} on ψ is significant, then interfacial fracture energy values should always be quoted together with the corresponding phase angle, since ψ values vary widely between different test procedures for measurement of G_{ic} and are also affected by the presence of residual stresses. (Note that residual stress states that are relaxed by the substrate and deposit bending away from each other give rise to mode I loading at the crack tip, while those relaxed by the two constituents changing their length generate mode II loading.) Experimental data for G_{ic} as a function of ψ are in short supply. Those available (Ref 59, 60) suggest that, while there is a general tendency for G_{ic} to rise with increasing ψ, the rise is much more significant when at least one of the constituents is metallic, and this may be related to the ease with which plastic flow can be promoted. This is an area requiring further experimental study.

4.3 *Debonding under Combined Residual and Applied Stresses*

In many cases, debonding occurs under the combined influence of residual stresses and those generated by the application of an external mechanical load. For example, there are both practical situations and testing procedures for measurement of interfacial toughness that involve the application of a bending moment to a coated substrate. The combined effect of such a moment and a set of residual stresses has been analyzed by Charalambides et al. (Ref 55, 61) and by Howard et al. (Ref 24). The stresses from the bending moment will superimpose on the residual stresses. However, the net strain energy release rate on debonding is not equal to the sum of the G values corresponding to the two sets of stresses in isolation. Furthermore, while any set of residual stresses, in isolation, can only promote (and not inhibit) debonding,* it is possible for residual stresses to interact with those from an applied load so that G would be lower than in their absence.

It can be shown (Ref 24) that the total strain energy release rate is given by:

$$G = \frac{P^2}{4b}\left(\frac{dC}{da}\right) + \frac{P}{2b}\left(\frac{du_r}{da}\right) + G_r \qquad \text{(Eq 20)}$$

where P is the applied load, b is the specimen width, C is the specimen compliance, u_r is the residual displacement on unloading, and G_r is the release rate for relaxation of the residual stresses in isolation. The first term in Eq 20 is the standard expression for a specimen without residual stresses, G_p, while the second represents the interaction between applied and residual stresses, G_{pr}. While the parameters in Eq 20 needed for evaluation of G_p and G_{pr} can be found from a load-displacement plot, G can also be found via other measurements, using (Ref 24):

$$G = \frac{P^2 s^2}{8b}\left(\frac{1}{\Sigma_s} - \frac{1}{\Sigma_c}\right) - \frac{Ps}{2b}(\kappa_s - \kappa_c) + G_r \qquad \text{(Eq 21)}$$

where s is the distance between inner and outer loading points in the four-point bend test. The testing geometry is shown in Fig. 12.

Experimental data relating to debonding of thick, residually stressed coatings under applied load are shown in Fig. 13. These plots show how the three terms—G_p, G_{pr}, and G_r—vary with applied load during delamination testing of two ceramic-coated titanium specimens. For the boron carbide coating (Fig. 13a), the residual stresses, shown in Fig. 10(a), were relatively high. In the case of the zirconia coating (Fig. 13b), however, the residual stresses were quite low, primarily as a result of the extensive microcracking that occurs and the consequently low coating stiffness. These differences are reflected in the higher value of G_r for the boron carbide coating. Furthermore, a consequence of the different stress distributions for the two cases is that G_{pr} is positive in one case and negative in the other. The measured interfacial fracture energies, however, are similar in the two cases, which is consistent with the fact that the substrates were prepared in the same way and spraying conditions were broadly

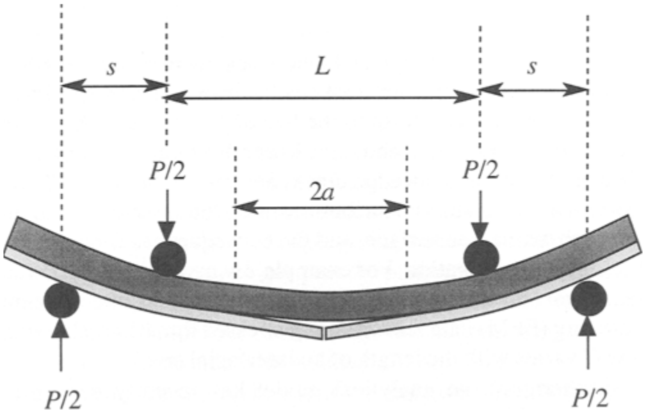

Fig. 12 Experimental arrangement for the four-point bend delamination test

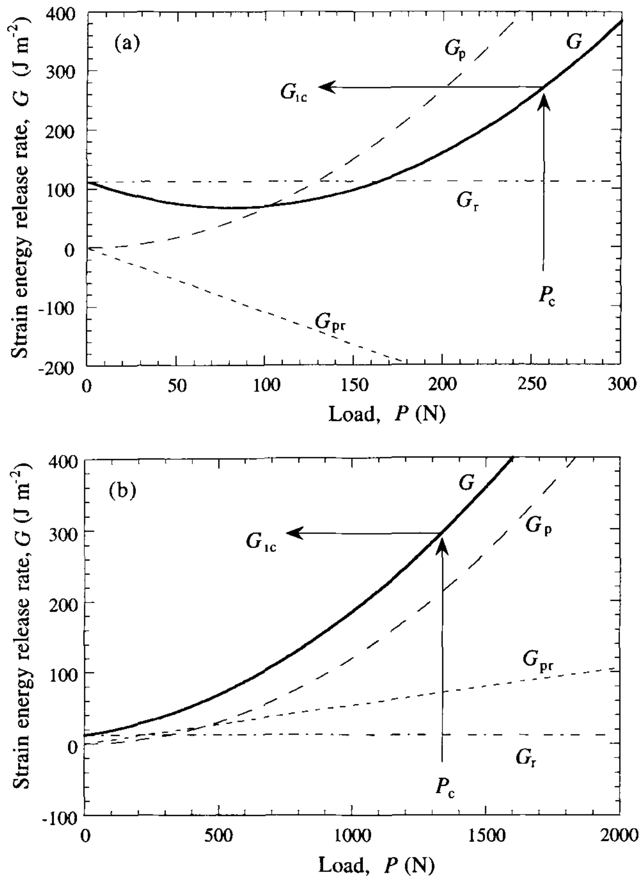

Fig. 13 (a) Variations of G_p, G_r, and G_{pr} with applied load during four-point bend delamination of a specimen of B_4C-coated titanium, having the residual stress distribution shown in Fig. 10(a). From the load at which interfacial crack propagation occurred, P_c, the interfacial fracture energy, G_{ic}, can be obtained. (b) Corresponding plots for a specimen of ZrO_2-coated titanium. Source: Ref 51

---

*Although this is true from the energy release point of view, there are at least two ways in which residual stresses could inhibit debonding. First, the phase angle could be changed so as to require higher energies for debonding; second, formation of through-thickness cracks in the coating (which can help to initiate debonding) could be inhibited by (compressive) residual stresses.

similar. It can be seen that neglect of the effect of residual stresses, or even just omission of the interaction term G_{pr}, would have led to significant errors for these systems. This is often expected to be the case.

4.4 *Initiation of Debonding and Effect of Crack Length*

It has long been recognized that, since the in-plane stress responsible for driving interfacial crack advance from a specimen edge must be relaxed close to the lateral free surface, the strain energy release rate will tend to be lower during the initial stages of the propagation of an edge crack. Several studies (Ref 62-68) have focused on stress distributions near the intersection of an interface with a free surface, and the consequences for crack initiation and propagation. For example, Evans et al. (Ref 63) and Akisanya and Fleck (Ref 64) have presented finite-element modeling (FEM) data for residually stressed thin films, showing how G varies with the length of an interfacial crack.

Furthermore, an analytical model has recently been presented (Ref 22) that allows an estimate to be made of the reduction in crack driving force near the specimen edge (or a through-thickness crack) for a coating on a massive substrate. By making a number of simplifying approximations, which were justified by comparison with FEM data, the following expression was derived for the dependence of strain energy release rate on the length, a, of a preexisting crack:

$$\frac{G(a)}{G_0} = \left(\frac{a}{hB}\right)^2 - \left(\frac{a}{hB}\right)\ln\left(\frac{a^2}{h^2 B^2}\right) \qquad \text{(Eq 22)}$$

where B is a dimensionless constant that can be evaluated from:

$$B = 10^{(\alpha + 1)} \qquad \text{(Eq 23)}$$

in which α is the Dundurs parameter, given by:

$$\alpha = \frac{E_d - E_s}{E_d + E_s} \qquad \text{(Eq 24)}$$

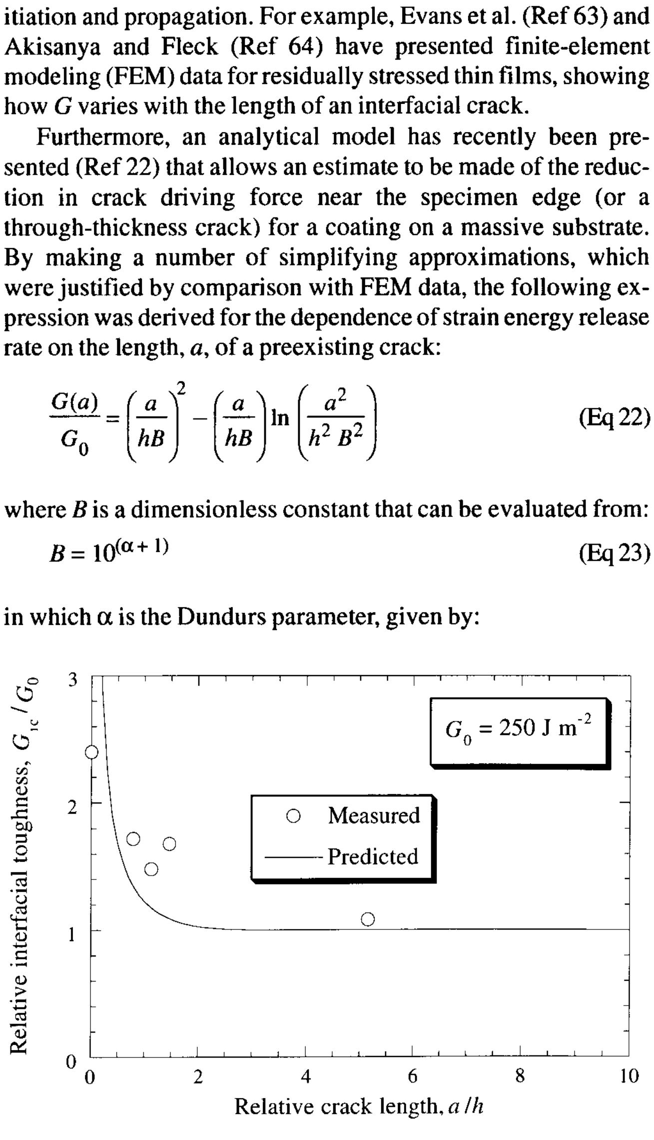

Fig. 14 Experimental data for the apparent interfacial toughness, G_{ic}, as a function of the length of artificial precrack for sprayed coatings of alumina on steel, obtained by monitoring the temperatures at which they underwent spontaneous debonding during postdeposition cooling. The predicted plot was obtained solely from effective stiffness values: $[E/(1-\nu)]_{steel} \sim 290$ GPa and $[E/(1-\nu)]_{Al_2O_3} \sim 90$ GPa (in the as-sprayed state), leading to $\alpha \sim -0.5$ (Eq 24) and $B \sim 3.2$ (Eq 23), which was then employed in Eq 22. Source: Ref 69

Use of Eq 22 to 24 therefore allows prediction of the effect of precrack length on the strain energy release rate for interfacial debonding initiated at an edge. However, it refers only to the case of a uniform misfit strain and a relatively thin deposit (massive substrate). Through-thickness stress gradients and/or a thick deposit would lead to curvature changes on debonding, which might complicate the issue.

Experimental data for apparent interfacial toughness as a function of edge precrack length are currently in very short supply. A study of this type was recently undertaken by Itoh and Clyne (Ref 69), although this was based on thermally sprayed coatings in which stress gradients were high and the deposits were relatively thick ($H \sim 3$ mm, $h \sim 1$ mm). Precracks were obtained by masking during grit blasting of the substrate, leaving highly polished regions in which proper interfacial bonding with the coating was never established. Interfacial toughnesses were inferred by measuring the temperatures at which alumina coatings debonded spontaneously from steel substrates during postdeposition cooling. Numerical process modeling (Ref 7, 30, 31) was used to obtain the stress distributions and hence the strain energy release rates. A comparison is shown in Fig. 14 between the apparent toughnesses measured in this way and the prediction given by the reciprocal of Eq 22. (A low crack driving force, $G(a)$, predicted for a short crack length, a, means that the measured toughness, $G_{ic}(a)$, will be large.) The predicted curve should obviously be capped at a crack size corresponding to the size of the extraneous flaws present at the interface near the edge. The data suggest that in this case flaws of $(a/h) \sim 1/4$ (i.e., $a \sim 200$ to 400 μm) were present. In view of the rather rough state of the edges of the specimens concerned, this is physically plausible.

The agreement between prediction and experiment shown in Fig. 14 is reasonable in view of the various approximations of the analysis and the differences between the experimental situation and that assumed in the model. There is a particular concern that the variations in mode mixity at debonding between individual specimens may have affected these results, and it is clear that further experimentation is necessary. Nevertheless, this treatment serves to highlight the fact that initiation of the spallation event can be quite strongly inhibited by such a reduction in driving force. In practice, it is probably common for coatings to be used in service having residual stress distributions and interfacial toughnesses such that steady-state propagation of an interfacial crack, once initiated, would be energetically favored.

5. Case Histories

5.1 *Edge Effects in Piston Crown and Piston Ring Coatings*

A simple example of the importance of edge effects on real industrial coatings is given by the experience of New Sulzer Diesel (NSD) during recent development activities to select protective coatings for application to marine diesel piston crowns (Ref 70). The conditions experienced by coatings applied to such crowns are extremely harsh, with thermal cycling damage, corrosion, and erosion all taking place simultaneously and synergistically. It is very difficult to reproduce these conditions in the laboratory, and coatings systems are normally tested in situ on real components. However, it is not always feasible to spray untested coatings over entire crowns, due to the excessive cost. Hence, the approach used by NSD has been to insert coated, 30 mm diam disks into matching recesses on the crown (Fig. 15), thus allowing several candidate systems to be studied in situ in a single engine test. Subsequent examination of the coatings is also made easier using this approach.

The technique has facilitated the successful development of piston crown coatings. However, the results must be interpreted with care. One of the best performing coatings tested using the disk method was a NiCr alloy that survived for approximately 3500 running hours without failure or significant corrosion/erosion damage. The alloy was then used to coat an entire (760 mm diam) piston crown; despite this earlier encouraging result, damage was observed after 2100 h, and catastrophic failure occurred after approximately 5000 h.

There are at least two possible explanations for this result. At the edges of both disk and crown, the radial in-plane stress component tends to zero, but this relaxation has greater consequences for the disk than for the crown because of the former's higher perimeter length to surface area ratio. In addition, the test disks contained several holes (necessary to allow them to be gripped while being screwed into and out of their recesses), at which the radial stresses must also decay to zero. The distance over which the stresses build up to their far-field value depends (Ref 64) on the residual stress state, the coating and substrate elastic properties, and the coating and substrate thicknesses (see section 4.4). However, if this decay distance is on the order of a few millimeters, then the stresses over large areas of the test disk would have been much lower than the stresses that were experienced by the coating on the crown. A second possible reason is simply that because of the greater surface area and edge perimeter length of the crown, there may have been a greater likelihood of the presence of critically sized flaws.

This example illustrates the effect that the reduction in residual stress may have at the edge of a coated component. To prolong lifetimes and increase reliability, this effect must be recognized and taken into account when finalizing the component design. This is illustrated by a further example, which concerns the various geometries of molybdenum and molybdenum-base self-fusing blend coatings sprayed by Goetze AG onto internal combustion engine piston rings. In Fig. 5, it can be seen that measured values of the quenching stress of molybdenum vary from 20 to 30 MPa for APS to 40 to 60 MPa for VPS. However, the former range is more applicable to the bulk of commercial coatings, which are generally produced by atmospheric processes such as APS or flame spraying. These values are surprisingly low, given the high melting point of molybdenum (2615 °C), but this can be at least partially explained by the (often deliberate) high oxygen content of sprayed coatings. Formation of MoO_2 hardens the coating (Ref 71), but also reduces its toughness and increases the likelihood of stress relief by microcracking and intersplat debonding. Residual stresses in molybdenum coatings arise mainly from differential thermal effects caused by the low expansion coefficient (compared with a cast iron or steel substrate) of only approximately 5×10^{-6} K^{-1}. The operational stress state is therefore sensitive to the difference between the substrate temperature during spraying and the component service temperature (Ref 72). During operation the coatings are also submitted to mechanical loads and influenced by the oil and fuel mixture. However, it has been shown (Ref 73) that the basic failure mechanisms of molybdenum coatings can be understood from an analysis of the thermal effects alone.

Buran et al. (Ref 74) have described in detail the various geometries that are used to produce molybdenum-base coatings on internal combustion engine piston rings. These can be divided essentially into the two categories of full-face and inlaid coatings (Fig. 16). Full-face coatings have the advantage of higher coating breakout resistance (see below), while the inlaid design permits a sharper peripheral edge, giving better control of blow-by (leakage of pressurized gas past the piston ring). The use of a particular design in a given application depends on the trade-off between these properties. Some rings are mixed, using a full-face coating on one side with an inlay on the other.

At the same operating temperature and away from the edges of the ring, both types of coatings will be approximately in an identical state of equal biaxial tension, with negligible through-thickness stresses. If coating breakout were mainly initiated away from the edges, there would be no difference in behavior between the two designs. As mentioned earlier, however, a strong influence *is* observed. The explanation for this can be understood from the schematic diagrams shown in Fig. 17. For simplicity, only the important features of the coating stress state are shown (stress singularities have been ignored) so that relative strain energy release rates can be estimated. It is clear that, in the inlaid design, the wall next to the coating permits the in-plane stresses to continue to the edge of the coating and that stresses in the through-thickness direction are also generated, while the full-face stress distribution will lead to a strain energy

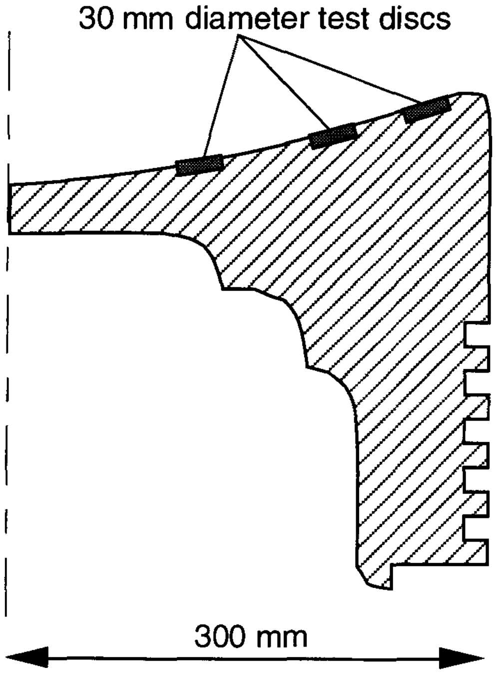

Fig. 15 Schematic showing recessed test disks inserted on a piston crown

release rate for interfacial edge crack growth in line with Eq 22. Thus, even though steady-state crack growth along the substrate/deposit interface away from the edges has the same value of strain energy release rate for both geometries, edge crack initiation is much easier for the inlaid coating. This contributes to its lower breakout resistance.

In practice, some of the worst effects are avoided by running the wall/coating interface at an angle to the surface (Fig. 16). This reduces the strain energy release rate for a given crack length and also promotes a stronger bond between coating and substrate, since the wall surface is better oriented with respect to the spray direction. The edges of full-face coatings are also chamfered, even though this increases blow-by, in order to reduce interfacial strain energy release rates.

5.2 *Stability of Zirconia Thermal Barrier Coatings*

Yttria-stabilized zirconia (YSZ) is widely used as a coating in the aerospace industry to give thermal barrier protection to surfaces exposed to high temperatures. Use in internal combustion engines is also increasing (Ref 75). Its chief advantages are its thermal stability, low thermal conductivity, and reasonably high thermal expansion coefficient of 7 to 10×10^{-6} K^{-1}. Because the coatings are relatively thick (at least ~300 μm is commonly applied) and are exposed to large thermal cycles, they must be able to withstand high strains induced by differential thermal expansion and thermal transients. A brief review of the approaches that have been used to obtain a high spallation resistance in YSZ thermal barrier coatings (TBCs) will serve to illustrate the various possibilities that are available to improve coating stability in general.

First, the composition of YSZ is controlled to produce a tough, spallation-resistant coating. The best results are obtained from a 6 to 8 wt% YSZ, which gives a metastable supersaturated tetragonal structure in the as-sprayed state (Ref 76). This structure has been termed "nontransformable" because of its good stability against decomposition into the cubic and monoclinic phases. It has also been observed that a reduction of silica impurities increases coatings lifetimes (Ref 77). These improvements, however, are specific to YSZ coatings. Of more general significance is the observation that coating lifetimes can be improved by increasing the porosity level— at least up to a certain level, beyond which the coating loses its integrity and becomes too friable. It is difficult to quantify coating porosity directly, but measurements of coating density have shown this effect (Ref 79). Increasing the porosity reduces the Young's modulus, which in turn lowers residual stress levels. In reality, however, the situation is more complicated because changes to the spraying parameters that affect the porosity level also affect microcracking and intersplat debonding, and these two are more effective at reducing the modulus than spherical porosity. Strain-tolerant electron-beam physical vapor deposition YSZ coatings are explicitly designed to make use of this effect through the development of a columnar-grained microstructure

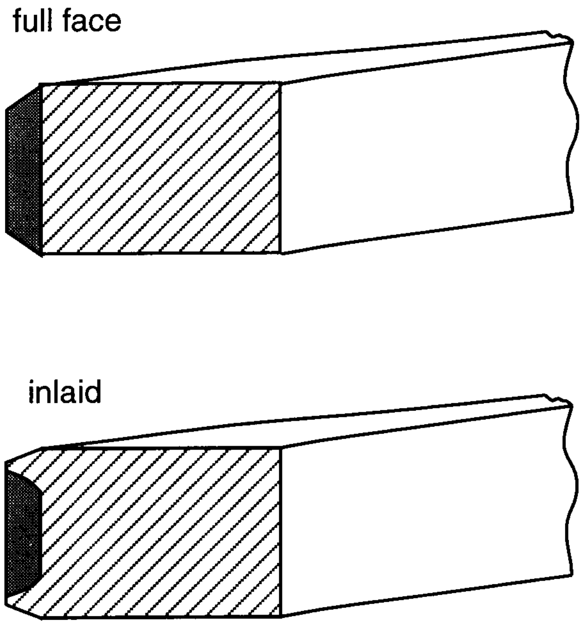

Fig. 16 Schematic showing full-face and inlaid piston ring coatings

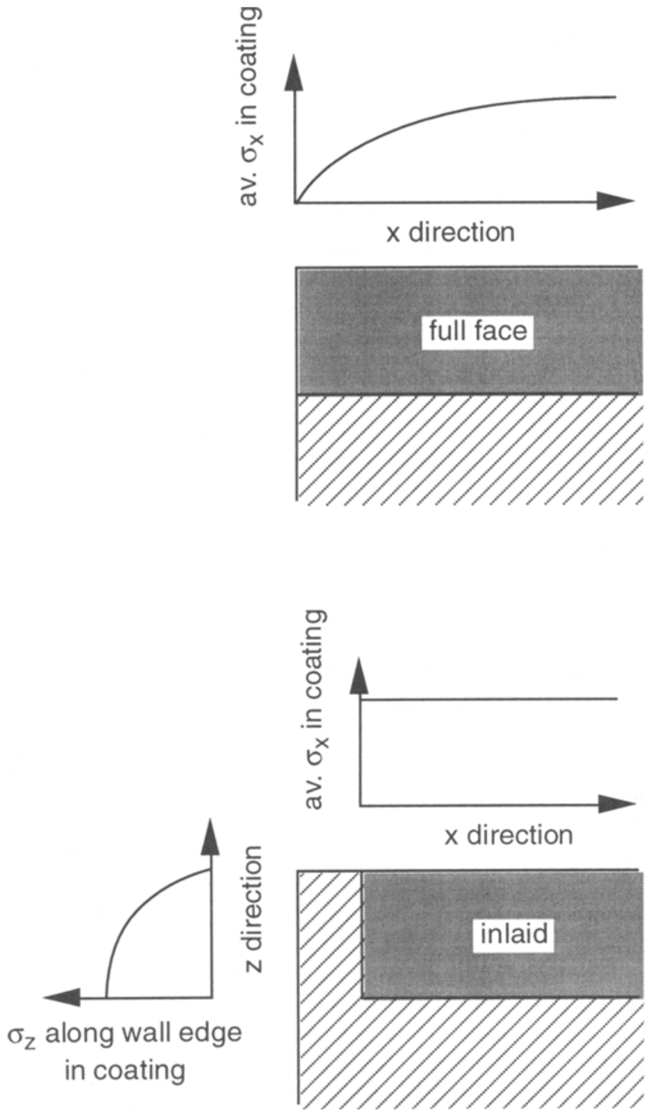

Fig. 17 Schematic of stress distributions in full-face and inlaid piston ring coatings

that permits a multitude of through-thickness segmentation cracks. Within each segment the in-plane stresses go to zero at the crack faces, and thus the available strain energy for substrate/deposit interfacial crack growth is greatly reduced. There is current interest in producing thermally sprayed ceramic coatings that also exhibit controlled segmentation, because of the increase in lifetime that can be obtained (Ref 80).

There are, of course, other reasons for encouraging porosity and microcracking in TBCs, not least of which is that it leads to a reduction in thermal conductivity. It is also possible that increased toughnesses can result from crack blunting effects. It is clear that the effects of porosity, cracking, and intersplat debonding on coating lifetime are complex. They cannot be considered in isolation, but must be optimized with respect to each other, the service conditions, and the probable coating failure mechanisms. In thermally sprayed YSZ coatings, this optimization process has led to the production of deposits with exceptional thermal shock resistance. Crack initiation, when it does occur, is often connected with oxidation of the bond coat.

5.3 *Function of Bond Coats and Interlayers*

Yttria-stabilized zirconia TBCs and other ceramic deposits are commonly sprayed with a bond coat. These are generally about 100 μm thick and are composed of thermally sprayed MCrAlY (where M can be nickel, cobalt, or iron, either singly or in some combination), although for other applications and with top coats other than zirconia, different metals or alloys can be used.

It is important for the bond coat to promote a stronger bond to the top coat—in other words, to increase the interfacial toughness. Data are available to confirm this effect. For example, Fig. 18 shows experimentally measured (Ref 81) toughnesses for various interfaces, including some that might form if an alumina oxidation barrier were introduced between the bond coat and the top coat. Such data, in combination with calculated strain energy release rates for debonding at the interfaces present during coating production and in service, will allow prediction of any spallation failure, although a complete analysis would also cover phase angle and crack initiation effects.

There is a widely held belief that, in addition to improving adhesion, the bond coat reduces the in-plane stresses in the top coat. In fact, such an effect can only be significant in the (admittedly important) vicinity of an edge or through-thickness crack. In most cases, the substrate has a significantly higher Young's modulus and is much thicker than either the bond or the top coat. Thus, except in the vicinity of edges and through-thickness cracks, strains (and hence stresses) in both the top coat and the bond coat will be almost entirely determined by the strain imposed by the substrate. Despite this observation, examples exist in the literature of attempts to control the average top coat stresses by altering the properties of the bond coat—for example, by applying a stiff bond coat (Ref 82).

In fact, assuming that the weakest interface of the system is the bond coat/top coat interface (see Fig. 18), the desirable properties of the optimum bond coat system are very simple to define. To remove the stress singularity at the edge of this interface requires a bond coat with exactly the same Young's modulus, Poisson's ratio, and coefficient of thermal expansion (CTE) as the top coat; that is, the bond coat should be of the same material as the top coat. (It should also be as thick as possible in order to distance the bond coat/top coat interface from the singular stress field originating at the substrate/bond coat interface.) This is, of course, an impracticable and trivial solution. A second solution is to completely decouple the coating from the substrate by having a bond coat with an effective modulus of zero. This is the idea behind the use of compliant interlayers, such as fiber metal pads or mats, which allow the production of very thick ceramic layers on metal substrates (Ref 83).

In reality, however, for most coatings a complex optimization has to be performed in order to balance the requirements of bond coat physical properties, and bond coat/substrate and bond coat/top coat interfacial toughnesses. To help this task, a J-integral calculation, similar to that performed by Akisanya and Fleck (Ref 64) for a single coating, could in principle be carried out to determine the strain energy release rate and mode mixity of a growing crack at the top coat/bond coat interface. This would require knowledge of all the relevant loadings and physical properties of the system, plus measured values of interfacial toughnesses for comparison. (See section 4.4 for a simpler analysis without a bond coat.) Results from this type of calculation have apparently not yet been published in the literature. Lee and Erdogan (Ref 84), however, have calculated the stress concentrations of TBC specimen edges submitted to a change in temperature both with and without bond coats, as well as for graded coatings (see below). As expected, their results show important reductions in stress intensity at the top coat/bond coat interface when bond coats of intermediate Young's modulus are used.

Other factors also have to be taken into account during the development of bond coats. A high bond coat/top coat interfacial roughness is important because a larger surface area increases the strain energy release rate needed to drive a crack along the interface. It also ensures that opposing crack surfaces interfere under mode II opening, effectively increasing the interfacial toughness still further (see section 4.2). Indeed, it has been observed that most cracks, once initiated, tend to grow, not along the interface, but in the top coat, close to and parallel to the bond coat/top coat interface (Ref 85). At high operating temperatures

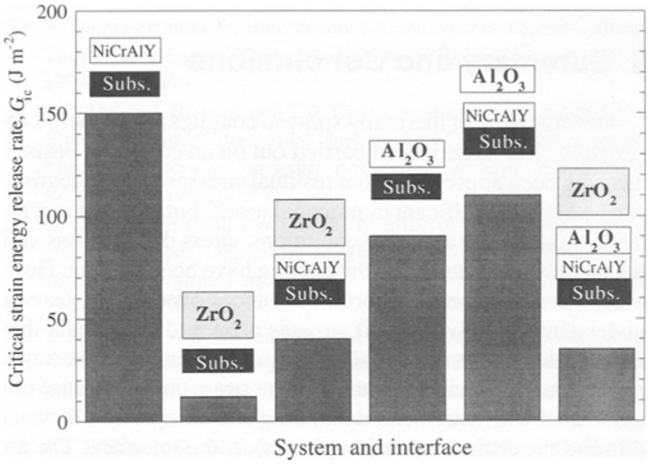

Fig. 18 Experimental data for interfacial toughness of various interfaces within multilayer TBCs. The schematic above each bar indicates the interface that was measured and the specimen geometry (subs. = substrate). Source: Ref 81

(>900 °C), NiCrAlY bond coats are also able to stress relax (Ref 86, 87) (see section 3.3), with beneficial effects on interfacial toughness at high temperature, but leading to increased coating edge stresses after cooling.

Finally, it is worth noting that, at least for TBC YSZ-MCrAlY systems, oxidation of the bond coat plays a central role in determining coating lifetime. Observation of interfacial delamination in these systems shows that cracking usually initiates in the alumina layer (Ref 88) that forms on the bond coat, and to grow further it deflects into the YSZ (Ref 85). If only in-plane biaxial stresses occurred in the coating and bond coat, there would be no driving force for these cracks to initiate. However, the interface is not smooth, and calculations show that microstresses with a tensile opening component perpendicular to the interface will occur at asperity tips in the oxide layer (Ref 85, 89).

In general, the presence of a bond coat cannot influence the average stresses in the top coat, except in the vicinity of edges and cracks. An exception to this relates to the use of graded structures, or multiple layers with intermediate CTEs, for use in situations where a thermal gradient exists across the coating. Brink (Ref 90) describes a thick TBC designed by Caterpillar Inc. for application to diesel engine piston crowns, where the CTEs of the various interlayers have been selected specifically to reduce the thermal mismatch strains produced by a given thermal gradient. However, such measures often result in increased oxidation rates. This is certainly a major problem with simply grading the transition from bond coat to top coat, since a larger surface area of bond coat is exposed to the oxidizing environment. In general, an oxidation barrier layer of some type is likely to be necessary.

With the exception of TBCs, however, loads (both physical and thermal) are usually applied to the same extent on all coating and substrate components. The role of a graded or multilayered structure is then to reduce stress concentrations on critical interfaces in the vicinity of edges and cracks. Indeed, Lee and Erdogan (Ref 84) have demonstrated that, by use of a fully graded structure, interfacial edge stress singularities are completely removed. This again takes no account of the probable degradation of oxidation resistance that commonly accompanies such grading.

6. Summary and Conclusions

Development of thermally sprayed coatings for industrial applications has largely been carried out on an empirical basis. It has long been appreciated that residual stresses in such coatings can be highly significant in practical terms, but detailed mechanistic links among spraying conditions, stress distributions, and the mechanical stability of the coating have been lacking. However, there have been important advances over recent years in understanding how residual stresses arise and the effects they have on the mechanical stability of sprayed coatings. The key to quantification lies in evaluation of the strain energy release rate associated with interfacial debonding and comparison between this and the critical value (toughness) of the interface. The approaches outlined in this paper show how current industrial design philosophies can be understood and rationalized in the light of a fracture mechanics approach to coating failure. Techniques for measurement and prediction of stress distributions and interfacial toughness can form the foundations of a systematic approach to coating design that should be used increasingly in the future.

Acknowledgments

Financial support for work on thermally sprayed coatings at Cambridge has been provided over recent years by the Engineering and Physical Sciences Research Council (U.K.). The authors would also like to acknowledge the value of extensive collaborations with Dr. S.J. Howard and Dr. Y.C. Tsui, both of the Department of Materials Science at Cambridge.

References

1. M.K. Hobbs and H. Reiter, Residual Stresses in ZrO_2-8%Y_2O_3 Plasma-Sprayed Thermal Barrier Coatings, *Surf. Coat. Technol.*, Vol 34, 1988, p 33-42
2. H. Zhuang and C. Gu, A Study on Residual Stress of ZrO + MgO Plasma Sprayed Coating, *Proc. 1st Plasma-Technik Symp.*, H. Eschnauer, P. Huber, A.R. Nicoll, and S. Blum-Sandmeier, Ed., Plasma-Technik, Wohlen, Switzerland, 1988, p 277-284
3. U. Selvadurai and W. Reimers, Characterisation of Phase Composition and Residual Stress State in Plasma Sprayed Ceramic Coatings, *High Performance Ceramic Films and Coatings*, P. Vincenzini, Ed., Elsevier, Amsterdam, 1990, p 319-328
4. D. Stover, D.A. Jager, and H.G. Schutz, Residual Stresses in Low Pressure Plasma Sprayed Chromia Coatings, *Proc. 4th National Thermal Spray Conf.*, T.F. Bernecki, Ed., Materials Information Society, 1991, p 215-219
5. R. Kingswell, K.T. Scott, and B. Sorensen, Measurement of Residual Stress in Plasma Sprayed Ceramic Coatings, *Proc. 2nd Plasma-Technik Symp.*, S. Blum-Sandmeier, H. Eschnauer, P. Huber, and A.R. Nicoll, Ed., Plasma-Technik, Wohlen, Switzerland, 1991, p 377-388
6. S.R. Brown, I.G. Turner, and H. Reiter, Residual Stress Measurement in Thermal Sprayed Hydroxyapatite Coatings, *J. Mater. Sci. Mater. Med.*, Vol 5, 1994, p 756-759
7. S.C. Gill and T.W. Clyne, Investigation of Residual Stress Generation during Thermal Spraying by Continuous Curvature Measurement, *Thin Solid Films*, Vol 250, 1994, p 172-180
8. D.S. Rickerby, K.T. Scott, and G. Eckold, Analysis of the Residual Stresses in Plasma Sprayed Coatings, *Proc. 1st Plasma-Technik Symp.*, H. Eschnauer, P. Huber, A.R. Nicoll, and S. Blum-Sandmeier, Ed., Plasma-Technik, Wohlen, Switzerland, 1988, p 267-276
9. R. Elsing, O. Knotek, and U. Balting, Calculation of Residual Thermal Stress in Plasma-Sprayed Coatings, *Surf. Coat. Technol.*, Vol 43/44, 1990, p 416-425
10. S. Takeuchi, M. Ito, and K. Takeda, Modelling of Residual Stress in Plasma-Sprayed Coatings: Effect of Substrate Temperature, *Surf. Coat. Technol.*, Vol 43/44, 1990, p 426-435
11. S.G. Gill, "Residual Stresses in Plasma Sprayed Deposits," Ph.D. thesis, University of Cambridge, U.K., 1991
12. J.D. Lee, H.V. Ra, K.T. Hong, and S.K. Hur, Analysis of Deposition Phenomena and Residual Stress in Plasma Spray Coatings, *Surf. Coat. Technol.*, Vol 56, 1992, p 27-37
13. D.J. Greving, E.F. Rybicki, and J.R. Shadley, Residual Stress Evaluations of Thermal Spray Coatings by a Modified Layer Removal Method, *Thermal Spray Industrial Applications*, C.C. Berndt and S. Sampath, Ed., ASM International, 1994, p 647-662
14. R. Elsing, O. Knotek, and U. Balting, The Influence of Physical Properties and Spraying Parameters on the Creation of Residual Thermal Stresses during the Spraying Process, *Surf. Coat Technol.*, Vol 41, 1990, p 147-156

15. S.C. Gill and T.W. Clyne, Property Data Evaluation for the Modelling of Residual Stress Development during Vacuum Plasma Spray Deposition, *1st European Conf. Advanced Materials and Processes (Euromat '89)*, H. Exner, Ed., Deutsche Gesellschaft für Metallkunde, Oberursel, Germany, 1990, p 1221-1230
16. E. Gheeraert, A. Deneuville, and A.M. Bonnot, Defects and Stress Analysis of the Raman Spectrum of Diamond Films, *Diamond Related Mater.*, Vol 1, 1992, p 525-528
17. J. Pina, A.M. Dias, V Costa, A. Goncales, M. Zaouali, and S.L. Lebrun, Residual Stresses in Plasma Sprayed Coatings, *Proc. 2nd Plasma-Technik Symp.*, S. Blum-Sandmeier, H. Eschnauer, P. Huber, and A.R. Nicoll, Ed., Plasma-Technik, Wohlen, Switzerland, 1991, p 99-108
18. M.T. Hutchings, Neutron Diffraction Measurement of Residual Stress Fields: Overview and Points for Discussion, *Measurement of Residual and Applied Stress Using Neutron Diffraction*, M.T. Hutchings and A.D. Krawitz, Ed., Kluwer Academic Publishers, 1992, p 3-20
19. I.B. Harris, J. Wright, D. Wang, L. Edwards, M.W. Johnson, and P.J. Withers, Surface Stress Measurements Made Using Neutron Diffraction, *J. Strain Anal.*, in press
20. P. Pantucek, E. Lugscheider, and U. Miller, Influence of Surface Temperature during Plasma Spraying on Residual Stresses in TBCs, *Proc. 2nd Plasma-Technik Symp.*, S. Blum-Sandmeier, H. Eschnauer, P. Huber, and A. Nicoll, Ed., Plasma-Technik, Wohlen, Switzerland, 1991, p 143-150
21. J. Lu, A. Niku-Lari, and J.F. Flavenot, Recents Developpements de la Mesure des Contraintes Residuelles par Percage Incremental, *Matér Tech. (Paris)*, 1985, p 709-718 (in French)
22. T.W. Clyne, Residual Stresses in Surface Coatings and Their Effects on Interfacial Debonding, *Key Eng. Mater.*, Vol 116/7, 1996, p 307-330

23 N.J. Salamon and C.B. Masters, Bifurcation in Isotropic Thin Film/Substrate Plates, *Int. J. Solids Struct.*, Vol 32, 1995, p 473-481

24. S.J. Howard, Y.C. Tsui, and T.W. Clyne, The Effect of Residual Stresses on the Debonding of Coatings, Part I: A Model for Delamination at a Bimaterial Interface, *Acta Metall. Mater.*, Vol 42, 1994, p 2823-2836
25. S. Kuroda, T. Kukushima, and S. Kitahara, In Situ Measurement of Coating Thickness during Thermal Spraying Using an Optical Displacement Transducer, *J. Vac. Sci. Technol.*, Vol A5, 1987, p 82-87
26. S. Kuroda, T. Kukushima, and S. Kitahara, Simultaneous Measurement of Coating Thickness and Deposition Stress during Thermal Spraying, *Thin Solid Films*, Vol 164, 1988, p 157-163
27. S. Gill and T.W. Clyne, Thermomechanical Modelling of the Development of Residual Stress during Thermal Spraying, *Proc. 2nd Plasma-Technik Symp.*, S. Blum-Sandmeier, P. Huber, A. Nicoll, and H. Eschnauer, Ed., Plasma-Technik, Wohlen, Switzerland, 1991, p 227-238
28. S.C. Gill and T.W. Clyne, Residual Stress Modelling and Characterisation of Thermally Sprayed Ceramic Coatings, *High Performance Ceramic Films and Coatings*, P. Vincenzini, Ed., Elsevier, Amsterdam, 1991, p 339-352
29. S.C. Gill and T W. Clyne, The Effect of Substrate Temperature and Thickness on Residual Stresses in Plasma Sprayed Deposits during Thermal Spraying, *2nd European Conf. Advanced Materials and Processes (Euromat '91)*, T.W. Clyne and P.J Withers, Ed., Institute of Materials, 1992, p 289-297
30. S.C. Gill and T.W. Clyne, Stress Distributions and Material Response in Thermal Spraying of Metallic and Ceramic Deposits, *Metall. Trans. B*, Vol 21B, 1990, p 377-385
31. T.W. Clyne and S.C. Gill, Heat Flow and Thermal Contraction during Plasma Spray Deposition, *Heat Transfer in Manufacturing and Processing of New Materials*, I. Tanasawa, Ed., Hemisphere, 1991, p 33-48
32. Y.C. Tsui, S.C. Gill, and T.W. Clyne, Simulation of the Effect of Creep on the Stress Fields during Thermal Spraying onto Titanium Substrates, *Surf. Coat. Technol.*, Vol 64, 1994, p 61-68
33. S. Kuroda and T.W. Clyne, The Quenching Stress in Thermally Sprayed Coatings, *Thin Solid Films*, Vol 200, 1991, p 49-66
34. S. Kuroda, T. Fukushima, and S. Kitahara, Significance of the Quenching Stress in the Cohesion and Adhesion of Thermally Sprayed Coatings, *13th Int. Conf. Thermal Spraying*, C.C. Berndt, Ed., ASM International, 1992, p 903-909
35. L. Pawlowski, *The Science and Engineering of Thermal Spray Coatings*, John Wiley & Sons, Chichester, U.K., 1995
36. S. Kuroda and T.W. Clyne, The Origin and Quantification of the Quenching Stress Associated with Splat Cooling during Spray Deposition, *Proc. 2nd Plasma-Technik Symp.*, H. Eschnauer, P. Huber, A. Nicoll, and S.B. Sandmeier, Ed., Plasma-Technik, Wohlen, Switzerland, 1991, p 273-284
37. S. Kuroda and T.W Clyne, The Quenching Stresses in Thermally Sprayed Coatings, *Thin Solid Films*, Vol 200, 1991, p 49-66
38. S.C. Gill and T.W Clyne, Monitoring of Residual Stress Generation during Thermal Spraying by Curvature Measurements, *Thermal Spray Industrial Applications*, C.C. Berndt and S. Sampath, Ed., ASM International, 1994, p 581-586
39. D.S. Rickerby, A Review of the Methods for the Measurement of Coating-Substrate Adhesion, *Surf. Coat. Technol.*, Vol 36, 1988, p 541-557
40. M.S. Hu, M.D. Thouless, and A.G. Evans, The Decohesion of Thin Films from Brittle Substrates, *Acta Metall.*, Vol 36, 1988, p 1301-1307
41. J.R. Rice, Elastic Fracture Mechanics Concepts for Interfacial Cracks, *J. Appl. Mech. (Trans. ASME)*, Vol 55, 1988, p 98-103
42. J.W. Hutchinson, "Mixed Mode Fracture Mechanics of Interfaces," Harvard Technical Report Mech-139, Division of Applied Sciences, Harvard University, 1989
43. M.-Y. He and J.W. Hutchinson, Kinking of a Crack out of an Interface, *J. Appl. Mech.*, Vol 56, 1989, p 270-278
44. A.G. Evans and J.W. Hutchinson, Effects of Non-planarity on the Mixed Mode Fracture Resistance of Bimaterial Interfaces, *Acta Metall.*, Vol 37, 1989, p 909-916
45. Z. Suo and J.W. Hutchinson, Interface Crack between Two Elastic Layers, *Int. J. Fract.*, Vol 43, 1990, p 1-18
46. A.G. Evans, M. Rühle, B.J. Dalgleish, and P.G. Charalambides, The Fracture Energy of Bimaterial Interfaces, *Mater. Sci. Eng.*, Vol A126, 1990, p 53-64
47. H.M. Jensen, The Blister Test for Interface Toughness Measurement, *Eng. Fract. Mech.*, Vol 40, 1991, p 475-486
48. A. Bartlett, A.G. Evans, and M. Rühle, Residual Stress Cracking of Metal/Ceramic Bonds, *Acta Metall. Mater.*, Vol 39, 1991, p 1579-1585
49. S.J. Howard and T.W. Clyne, Surface Preparation of Titanium for Vacuum Plasma Spraying and Its Effect on Substrate/Coating Interfacial Fracture Toughness, *Composites*, Vol 24, 1993, p 603-610
50. V. Tvergaard and J.W. Hutchinson, Toughness of an Interface along a Thin Ductile Layer Joining Elastic Solids, *Philos. Mag. A*, Vol 70, 1994, p 641-656
51. Y.C Tsui, S.J. Howard, and T.W. Clyne, Application of a Model for the Effect of Residual Stresses on Debonding of Coatings under Applied Loads, *Advances in Inorganic Films and Coatings*, P. Vincenzini, Ed., Elsevier, 1995, p 19-26
52. A. Itoh, S.C. Gill, and T.W. Clyne, The Effect of Cooling Conditions on the Spontaneous Debonding of Thermally Sprayed Coatings, *Advances in Inorganic Films and Coatings*, P. Vincenzini, Ed., Elsevier, 1995, p 451-458
53. D.K. Shetty, A.R. Rosenfield, and W.H. Duckworth, Mixed-Mode Fracture in Biaxial Stress State: Application of the Diametral-Compression (Brazilian Disk) Test, *Eng. Fract. Mech.*, Vol 26, 1987, p 825-840
54. J.G. Williams, On the Calculation of Energy Release Rates for Cracked Laminates, *Int. J. Fract.*, Vol 36, 1988, p 101-119
55. M. Charalambides, A.J. Kinloch, Y. Wang, and J.G. Williams, On the Analysis of Mixed-Mode Failure, *Int. J. Fract.*, Vol 54, 1992, p 269-291

56. I.E. Reimanis, B.J. Dalgleish, and A.G. Evans, The Fracture Resistance of a Model Metal/Ceramic Interface, *Acta Metall. Mater.*, Vol 39, 1991, p 3133-3141
57. M.D. Thouless, Mixed-Mode Fracture of a Lubricated Interface, *Acta Metall. Mater.*, Vol 40, 1992, p 1281-1286
58 V. Tvergaard and J.W. Hutchinson, The Influence of Plasticity on Mixed Mode Interface Toughness, *J. Mech. Phys. Solids*, Vol 41, 1993, p 1119-1135
59. A.R. Akisanya and N.A. Fleck, Brittle Fracture of Adhesive Joints, *Int. J. Fract.*, Vol 58, 1992, p 93-114
60. A.J. Phillips, W.J. Clegg, and T.W. Clyne, Fracture of Ceramic Laminates in Bending, Part II: Comparison of Model Predictions with Experimental Data, *Acta Metall. Mater.*, Vol 41, 1993, p 819-827
61. P.G. Charalambides and A.G. Evans, Debonding Properties of Residually Stressed Brittle Matrix Composites, *J. Am. Ceram. Soc.*, Vol 72, 1989, p 746-753
62. J.W. Hutchinson and Z. Suo, Mixed Mode Cracking in Layered Materials, *Adv. Appl. Mech.*, Vol 29, 1991, p 63-191
63. A.G. Evans, M.D. Drory, and M.S. Wu, The Cracking and Decohesion of Thin Films, *J. Mater. Res.*, Vol 3, 1988, p 1043-1049
64. A.R. Akisanya and N.A. Fleck, The Edge Cracking and Decohesion of Thin Films, *Int. J. Solids Struct.*, Vol 31, 1994, p 3175-3199
65. D. Munz and Y.Y. Yang, Stress Singularities at the Interface in Bonded Dissimilar Materials under Mechanical and Thermal Loading, *J. Appl. Mech.*, Vol 59, 1992, p 857-861
66. D. Munz, M.A. Sckuhr, and Y.Y. Yang, Thermal Stresses in Ceramic-Metal Joints with an Interlayer, *J. Am. Ceram. Soc.*, Vol 78, 1995, p 285-290
67. S. Ho, C. Hillman, F.F. Lange, and Z. Suo, Surface Cracking in Layers under Biaxial, Residual Compressive Stress, *J. Am. Ceram. Soc.*, in press
68. J.L. Beuth, Cracking of Thin Bonded Films in Residual Tension, *Int. J. Solid Struct.*, Vol 29, 1992, p 1657-1675
69. A. Itoh and T.W. Clyne, Initiation and Propagation of Interfacial Cracks during Spontaneous Debonding of Thermally Sprayed Coatings, *Advances in Thermal Spray Science and Technology*, C.C. Berndt and S. Sampath, Ed., ASM International, 1995, p 425-431
70. D. Schlager, private communication
71. S. Sampath, V. Anand, and S.F. Wayne, On the Properties of Mo-based Thermal Spray Coatings for Piston Ring Applications, *Proc. 2nd Plasma-Technik Symp.*, S. Blum-Sandmeier, H. Eschnauer, P. Huber, and A.R. Nicoll, Ed., Plasma-Technik, Wohlen, Switzerland, 1991, p 279-288
72. U. Buran and M. Fischer, Fundamental Considerations on the Use of Graded Coatings—Piston Ring Wear Surfaces, *Proc. 2nd Plasma-Technik Symp.*, S. Blum-Sandmeier, H. Eschnauer, P. Huber, and A.R. Nicoll, Ed., Plasma-Technik, Wohlen, Switzerland, 1991, p 195-206
73. H. Beyer and H.J. Neuhäuser, "SEM Studies of Cracking in Thermally Sprayed Piston Rings," Report K20, Goetze AG, Bursheid, Germany, 1994
74. Y. Buran, H.-C. Mader, M. Morsbach, and B.A. Newman, Plasma-Sprayed Coatings for Piston Rings—State of Development and Application Potential, *Proc. Conf. Surface Modifications and Coatings*, ASM International, 1985, p 255-265
75. W.J. Brindley and R.A. Miller, TBCs for Better Engine Efficiency, *Adv. Mater. Proc.*, Vol 136, 1989, p 29-33
76. D.S. Suhr, T.E. Mitchell, and R.J. Keller, Microstructure and Durability of Zirconia Thermal Barrier Coatings, *2nd Int. Conf. Science and Technology of Zirconia*, N. Claussen, M. Ruhle, and A.H. Heuer, Ed., American Ceramic Society, 1984, p 503-517
77. R.A. Miller, W.J. Brindley, J.G. Goedjen, R. Tiwari, and D. Mess, The Effect of Silica on the Cyclic Life of a Zirconia-Yttria Thermal Barrier Coating, *Proc. 7th National Thermal Spray Conf.*, C.C. Berndt and S. Sampath, Ed., ASM International, 1994, p 49-56
78. B.A. Movchan, I.S. Malashenko, K.Y. Yakovchuk, A.I. Rybnikov, and A.A. Tchizhik, Two- and Three-Layer Coatings Produced by Deposition in Vacuum for Gas Turbine Blade Protection, *Surf. Coat. Technol.*, Vol 67, 1994, p 55-63
79. R.A. Miller, Current Status of Thermal Barrier Coatings—An Overview, *Surf. Coat. Technol.*, Vol 30, 1987, p 1-11
80. H. Nakahira, Y. Harada, N. Mifune, T. Yogoro, and H. Yamane, Advanced Thermal Barrier Coatings Involving Efficient Vertical Microcracks, *J. Therm. Spray Technol.*, Vol 2, 1993, p 51-57
81. Y.C. Tsui and T.W. Clyne, Adhesion of Thermal Barrier Coating Systems and Incorporation of an Oxidation Barrier Layer, *Thermal Spray: Practical Solutions for Engineering Problems*, C.C. Berndt, Ed., ASM International, 1996, p 275
82. J.C. Lutz and D.H. Harris, Development of Thermal Barrier Coatings for the Internal Combustion Engine, *Proc. Conf. Thermal Spray Technology: New Ideas and Processes*, ASM International, 1988, p 437-444
83. G.P. Jarrabet, Compliant Interlayer for Advanced Ceramic/Metal Engine Components, *Auto. Eng.*, 1995, p 29-32
84. Y.-D. Lee and F. Erdogan, Residual Thermal Stresses in FGM and Laminated Thermal Barrier Coatings, *Int. J. Fract.*, Vol 69, 1994, p 145-165
85. A.H. Bartlett and R.D. Maschio, Failure Mechanisms of a Zirconia-8%Yttria Thermal Barrier Coating, *J. Am. Ceram. Soc.*, Vol 78, 1995, p 1018-1024
86. W.J. Brindley and J.D. Whittenberger, Stress Relaxation of Low Pressure Plasma Sprayed NiCrAlY Alloys, *Mat. Sci. Eng.*, Vol A163, 1993, p 33-41
87. M.G. Hebsur and R.V. Miner, Stress Rupture and Creep Behavior of a Low Pressure Plasma-Sprayed NiCoCrAlY Coating Alloy in Air and Vacuum, *Thin Solid Films*, Vol 147, 1987, p 143-152
88. F. Bordeaux, R.G.S. Jacques, C. Moreau, S. Dallaire, and J. Lu, Thermal Shock Resistance of TiC Coatings Plasma Sprayed onto Macroroughened Substrates, *Surf. Coat. Technol.*, Vol 53, 1992, p 49-56
89. G.C. Chang, W. Phucharoen, and R.A. Miller, Behaviour of Thermal Barrier Coatings for Advanced Gas Turbine Blades, *Surf. Coat. Technol.*, Vol 30, 1987, p 13-28
90. R.C. Brink, Material Property Evaluation of Thick Thermal Barrier Coating Systems, *J. Eng. Gas Turbines Power (Trans. ASME)*, Vol 111, 1989, p 570-577